

RESEARCH ARTICLE

10.1029/2020JD032384

Key Points:

- Different subregions near the updraft core of a developing supercell contained markedly different vertical charge structures
- Retrieved mean graupel trajectories often moved horizontally around or through the updraft rather than entering the subregions from below
- Retrieved estimates of the microphysics graupel experienced along these trajectories hint at reasons for the different charge structures

Supporting Information:

- Supporting Information S1

Correspondence to:

V. C. Chmielewski,
vanna.chmielewski@noaa.gov

Citation:





Chmielewski, V. C., MacGorman, D. R., Ziegler, C. L., DiGangi, E., Betten, D., & Biggerstaff, M. (2020). Microphysical and transportive contributions to normal and anomalous polarity subregions in the 29–30 May 2012 Kingfisher storm. *Journal of Geophysical Research: Atmospheres*, 125, e2020JD032384. <https://doi.org/10.1029/2020JD032384>

Received 6 JAN 2020

Accepted 30 JUN 2020

Accepted article online 3 JUL 2020

Microphysical and Transportive Contributions to Normal and Anomalous Polarity Subregions in the 29–30 May 2012 Kingfisher Storm

Vanna C. Chmielewski^{1,2} , Donald R. MacGorman^{1,2,3} , Conrad L. Ziegler^{2,3}, Elizabeth DiGangi^{1,2} , Daniel Betten⁴, and Michael Biggerstaff³ 

¹Cooperative Institute for Mesoscale Meteorological Studies, University of Oklahoma, Norman, OK, USA, ²NOAA/OAR National Severe Storms Laboratory, Norman, OK, USA, ³School of Meteorology, University of Oklahoma, Norman, OK, USA, ⁴CoreLogic, Inc., Irvine, CA, USA

Abstract A developing supercell storm on 29–30 May 2012 in north-central Oklahoma was observed with the Oklahoma Lightning Mapping Array (OKLMA) and three mobile radars. The storm's vertical charge structure inferred from the OKLMA was anomalous overall but varied considerably even within 10 km of the bounded weak echo region (BWER) and the bounded weak lightning region (BWL) or lightning hole. Near the BWER, three distinct charge structures were observed—an inverted dipole, an inverted tripole, and a bottom-heavy normal tripole. One column within each structure was analyzed relative to the Doppler-derived wind field and environmental properties derived by a diabatic Lagrangian analysis (DLA). Within each column, back trajectories of graupel and hail particles additionally illustrate the history of the diagnosed in-cloud microphysical properties, which are expected to influence noninductive electrification and may have contributed to the observed charge profiles. This study objectively demonstrates the complicated scenarios presented by the three-dimensional motions around and through the updraft and provides likely constraints on how each of the three distinct vertical charge distributions could have been produced within this focused region of the storm.

Plain Language Summary This study analyzes in detail the unusual distribution of lightning-containing layers and inferred charge structures near the updraft core of a single storm, with a focus on three different columns representing the distinctly different vertical charge structures found at a single point in time. One of these charge structures was relatively normal, while two were anomalous. We use a retrieval technique that derives properties of different cloud particles such as graupel, snow, and cloud water droplets from storm observations and the background environment. We then examine the paths that the average particles likely followed to carry charge through the storm into each of these columns. We know that lightning ultimately is caused by the charge separated by large numbers of frozen particles colliding and moving apart in certain environmental conditions, so this novel analysis allows us to investigate when average particles in each unique region passed through conditions favorable for electrification.

1. Introduction

Supercell charge structures, the vertical distribution of net charge or the electrical potential controlling lightning discharges, can become notoriously complex (e.g., Brothers et al., 2018; Bruning et al., 2010; Calhoun et al., 2013; Stolzenburg et al., 1998). Even so, the charge structure near the updraft region is relatively simple, as hydrometeors were recently generated and electrified before complex redistribution by storm motions (Lang et al., 2004; MacGorman et al., 2005; Stolzenburg et al., 1998).

Charge distributions can be complicated by local or temporal variations in hydrometeor electrification due to environmental changes. The most efficient generator of thunderstorm charge is the noninductive (NI) collisional charge exchange between rebounding graupel and ice crystals in the presence of supercooled liquid water (SLW) (Illingworth & Latham, 1977; Saunders et al., 2006; Takahashi, 1978). The polarity of charge separated on each rebounding hydrometeor varies with the surrounding environment and the relative growth rate of each (Baker et al., 1987; Emersic & Saunders, 2010). Environments with temperatures greater than roughly -10°C or abundant SLW generally favor graupel gaining a net positive charge and ice crystals

net negative charge. The reverse occurs in colder or more liquid-starved environments (as summarized by Saunders et al., 2006).

The three main charge regions within a *normal* charge structure are readily explained by NI charging in environmental conditions, which describe a typical storm updraft. Graupel and ice particles interacting at warmer temperatures in the mixed-phase updraft region (0°C to -40°C) produce a positive graupel-negative ice pair, while particles interacting at colder temperatures, with moderate liquid water contents higher in the updraft, produce the opposite polarities. After differential sedimentation this electrification pattern produces the normal three-layer or “tripole” structure with net negative charge at midlevels (-10°C to -30°C) and net positive below and above (Illingworth & Latham, 1977; Takahashi, 1978). In this idealized structure, intracloud flashes between the upper-level positive charge and midlevel negative charge would be described as positive (+ICs), and those between the midlevel negative charge and the lower positive would be described as negative (-ICs). This structure would additionally be expected to produce cloud-to-ground flashes, which lower negative charge to ground (-CGs; the reverse would be a +CG) as consistently observed throughout the historical record (e.g., Brook et al., 1982; Simpson & Robinson, 1941).

Storms can also produce positive charge at midlevels with negative charge aloft via NI electrification in different environmental conditions than outlined above, thus forcing an *inverted* or *anomalous* structure that promotes more upper-level -ICs and +CGs (Krehbiel et al., 2008; Marshall & Stolzenburg, 2002; Rust et al., 2005). Maintaining large SLW content throughout depths supporting mixed-phase precipitation favors positive graupel and negative ice crystal electrification by NI collisional charging and therefore promotes deep positive charge in the midlevels (Bruning et al., 2014; MacGorman et al., 2005; Saunders et al., 2006). Significant SLW content likely contributes to the observed storm cases producing both anomalous characteristics and large hail (Carey & Rutledge, 1998; MacGorman & Burgess, 1994). While conditions would be thought to favor riming, not all anomalous storms support the growth of large hail (e.g., Chmielewski et al., 2018; Rust & MacGorman, 2002; Tessorodorf et al., 2007), which may be the result of limited trajectories favorable for hail growth or reflect the uncertainties in the hypotheses surrounding NI charging mechanisms.

There is still a significant amount of uncertainty surrounding NI electrification. The laboratory studies do not precisely agree, as well described by Saunders et al. (2006). They do generally agree that relatively warm, moist environments support positive graupel electrification, so that will be the focus of discussion in this manuscript, with the acknowledgement that the precise temperature and moisture characteristics that result in either positive or negative graupel electrification are debated (e.g., Saunders & Peck, 1998; Takahashi, 1978). There are many additional factors that can also influence electrification: Particle roughness can affect the relative growth rate of hydrometeors and by extension the polarity of charge transferred in collisions (e.g., Avila et al., 2005; Glassmeier et al., 2018; Tsenova & Mitzeva, 2009); impact velocity may also be a factor, as included in rime accretion rate-controlled laboratory studies (e.g., Brooks et al., 1997; Saunders & Peck, 1998); and electrification at low water content is under active investigation (e.g., Dye & Bansemer, 2019; Luque et al., 2016).

Enhanced SLW content and anomalous electrification is thought to be favored in storms having less efficient warm rain processes in the updraft (Williams et al., 2005), unusually fast updrafts (Fuchs et al., 2015; MacGorman et al., 2005), constrained recirculation of embryonic frozen cloud ice into the updraft core (MacGorman et al., 2011), and limited entrainment (Fuchs et al., 2018). However, these properties may change rapidly outside of the updraft core where weaker upward motions contain more embryonic ice-phase particles to scavenge SLW. Horizontally decreasing SLW and temperature due to decreasing bulk cloud condensation owing to increasing elevation of the effective updraft parcel inflow layer base and its associated lifted condensation level (LCL) may also limit contiguous areas supporting horizontally homogeneous electrification. If homogeneous charge regions are not created, the spatial extent of a single bidirectional lightning flash may be limited, as channel propagation is controlled by the wells of electric potential (e.g., Bruning & MacGorman, 2013; Coleman et al., 2003; MacGorman et al., 2001). High flash rates are common in areas with small flashes, where the limited volumes of electric potential and likely rapid charge replenishment result in scattered locations with large electric fields to initiate flashes, even after a single flash discharges any small electric potential imbalance (Bruning & MacGorman, 2013). It is especially important to understand how such factors and high rates of small flashes vary temporally, as they could

influence storm-scale metrics such as lightning jumps, an important consideration for the operational use of lightning data (Chronis et al., 2015; Schultz et al., 2015).

This study examines regions of charge polarity inferred from the Oklahoma Lightning Mapping Array (OKLMA MacGorman et al., 2008; Thomas et al., 2004) and cloud environmental characteristics derived from a diabatic Lagrangian analysis (DLA DiGangi et al., 2016; Ziegler, 2013a, 2013b) within and near the main updraft of the 29–30 May 2012 storm near Kingfisher, Oklahoma. The Kingfisher supercell was characterized in an overall sense by an anomalous charge structure (DiGangi et al., 2016) but contained subregions near the updraft core characterized by either normal or inverted polarity charge profiles, as will be shown. This manuscript will first document the overall characteristics and temporal variability of three subregions, with special attention to contained areas of updraft that might promote additional, local electrification of preexisting hydrometeors. DLA-derived mass-weighted graupel/hail trajectories passing through vertical columns in each lightning-producing subregion were next identified at a single point in time. The manuscript examines the histories of local in situ cloud state following these trajectories as a preliminary test of the microphysical charging pathways followed within the core of this single storm. Discussion will focus on the fundamental factors that modulate NI charging including the (DLA-derived) temperature, SLW content, and concentrations of smaller unrimed snow and cloud ice particles. Additional, follow-on research would be needed to further test the electrification hypotheses within each substructure.

2. Methodology

The Deep Convective Clouds and Chemistry field campaign (Barth et al., 2015) collected data on the 29–30 May 2012 storm near Kingfisher, Oklahoma, as it intensified and formed supercellular characteristics (DiGangi et al., 2016). The data collected by two Shared Mobile Atmospheric Research and Teaching Radars (SMART-Radars) (Biggerstaff et al., 2005), the NSSL X-band radar (Burgess et al., 2010), and the OKLMA (MacGorman et al., 2008; Thomas et al., 2004) are the foundation of this study. Complete description of the sample period and data processing can be found in DiGangi et al. (2016) and DiGangi (2019). The morphology and evolution of kinematic, microphysical, electrical, and lightning fields during the 21-min time period 2342–0003 UTC are described in detail in the present study. This time period was toward the end of the observation period during storm intensification and prior to several severe hail reports following 0000 UTC (DiGangi et al., 2016).

The wind field has been derived with a variational dual-Doppler analysis method (DiGangi et al., 2016; Potvin et al., 2012; Shapiro et al., 2009). The full set of 3-D wind analyses is published in DiGangi et al. (2016), but pertinent details of the method are included here. The radar analysis spatial domain is discretized with a 0.5-km grid spacing in all directions and a domain size of 120 km west-east, 80 km (south-north), and 0.2 to 17.7 km AGL or 0.575 to 18.075 km MSL in the vertical (all altitudes henceforth are MSL). The radar analyst optionally elected to locate the lowest grid level at 0.2 km AGL to more closely approximate the lowest radar scan elevation. Radar analyses are spaced at 3-min intervals from 2251 UTC on 29 May to 0000 UTC on 30 May 2012. To generate these analyses, the full volume of data from each 3-min mobile radar scan was interpolated with a natural neighbor scheme (e.g., Alford et al., 2019; Sibson, 1981) to the three-dimensional Cartesian grid. The interpolation procedure included a correction for advection due to storm motion: The u and v components of storm motion for each case were calculated via manual inspection in SOLO3 (Oye et al., 1995) and then assigned in the interpolation procedure using the same method as Alford et al. (2019). For each volume scan, the pair of mobile radars providing the most favorable dual-Doppler observing geometry covering the storm at that time were used to retrieve the 3-D wind field from the interpolated data using the 3DVAR analysis procedure outlined by Potvin et al. (2012) with an automated optimization of the cost function with respect to mass conservation (e.g., Alford et al., 2019; DiGangi, 2019; routine available at <https://github.com/nasa/MultiDop>). As discussed by Potvin et al. (2012), the 3DVAR method offers several advantages over traditional 3-D wind retrievals (e.g., Gao et al., 1999). The most prominent advantage is that, because it does not explicitly integrate the equation of mass continuity in the vertical, it is more flexible than traditional methods and less susceptible to the errors inherent in them.

The diabatic Lagrangian analysis (DLA) assimilates the time-spaced 3-D radar analyses via a multistep process, the first step being a diagnosis of the time-dependent rain, snow, and graupel/hail mixing ratio fields within the gridded radar analysis domain. Grid point values of precipitation particle total concentrations

and mean diameters are derived from gridded mixing ratios and assumed inverse-exponential size distribution intercept parameter values. The second DLA step involves the generation of backward-in-time air trajectories from all analysis grid points into the storm inflow environment, followed by initialization of each inflow trajectory with pressure, potential temperature, and water vapor mixing ratio profiles from the 0020 UTC 30 May 2012 environmental sounding. In the final DLA step a set of ordinary differential conservation equations for heat and water substance is integrated forward in time along each air trajectory from their prescribed initial conditions to explicitly predict the Lagrangian evolutions of potential temperature and the mixing ratios of water vapor, cloud water, and cloud ice (DiGangi et al., 2016; Ziegler, 2013a; 2013b). The time-spaced DLA analysis fields are composed of the diagnosed precipitation fields combined with the final (Lagrangian) analysis grid point values of predicted heat and water substance.

Similar radar analyses and thermal-microphysical continuity retrievals have previously been validated in detail using independent in situ observations (e.g., Ziegler et al., 1986, 1991). For example, Ziegler et al. (1991) showed that the time-varying radar-analyzed vertical velocities were within less than $\sim 4 \text{ m s}^{-1}$ of the measured NCAR-NOAA sailplane in situ measurements at the same times and locations. Similarly, Ziegler et al. (1986, 1991) showed that retrieved microphysical quantities were in similarly good agreement with the independent in situ sailplane measurements.

The OKLMA continually interrogates flash characteristics by determining the times of peaks of very high frequency (VHF) radiation along lightning channels and using the times to calculate the source of the radiation (MacGorman et al., 2008; Thomas et al., 2004). The storm remained within 105 km of the central OKLMA cluster where flash detection efficiency is estimated to be $\geq 98\%$ and the standard deviation of vertical errors $< 0.2 \text{ km}$ (Chmielewski & Bruning, 2016). Flash-level characteristics were computed with the open-source *lmatools* package (Fuchs et al., 2015). Flashes were required to contain at least 10 VHF sources, each received by at least six stations with reduced chi-square values ≤ 1 . Sources added to a flash were required to be within 3 km and 0.15 s of the previous source, and the resulting flashes were limited to a max duration of 3 s (following Fuchs et al., 2015). Flash products (i.e., flash extent density and flash initiation locations) were computed on the same 0.5-km grid as the radar analysis. All plots showing individual VHF sources are limited to those with at least seven contributing stations to reduce noise but preserve features such as overshooting top signatures that might be removed by the flash grouping.

The polarity of breakdown in individual flashes has been assigned by the standard subjective method (e.g., Coleman et al., 2003; Rust et al., 2005) following the bidirectional flash model (Kasemir, 1960; Mazur & Ruhnke, 1993; Rison et al., 2016). Breakdown is assumed to begin at a point with a large electric field (Shao & Krehbiel, 1996) and propagate through channels of negative breakdown into regions of positive electric potential and vice versa (Coleman et al., 2003; MacGorman et al., 1981, 2001; Williams et al., 1985). The negative breakdown process typically emits more frequent and higher power VHF source points (Thomas et al., 2001) and propagates faster (van der Velde & Montanyà, 2013) than positive breakdown. Additionally, the direction of initial propagation is often toward positive potential and likely net positive charge (Maggio et al., 2005; Shao & Krehbiel, 1996). Only VHF sources that could be identified as part of channel breakdown according to this model were assigned a polarity. Accumulated flashes associate with concentrated net charge regions, which corresponds well with in situ observations (e.g., Lang et al., 2004; Lund et al., 2009; MacGorman et al., 2005; Rust et al., 2005). Note that although channel propagation is more specifically related to the spatial distribution of electric potential, the potential is often simply assumed to be the result of large regions of net charge. The terminology of a subregion possessing a “net charge” will be used for consistency with previous work, with the understanding that the details of full distributions of net charge are more complex than one would infer from this analysis (Brothers et al., 2018; Coleman et al., 2003).

Additional backward-in-time, bulk trajectories for snow and graupel/hail precipitation particles (i.e., the precipitation particle types that in addition to cloud ice are known to participate in NI electrification and macroscopic charge transport) are generated from the radar analysis and DLA fields including the effect of precipitation on net vertical displacement relative to the air motion (Figures 1a and 1b). The calculated bulk trajectories of graupel/hail and snow incorporate their respective mass-weighted fall speeds (Straka & Mansell, 2005), while cloud ice is assumed to be transported as a passive tracer of the airflow via the air trajectories calculated in the DLA. Each trajectory calculation employs a 10-s time step and three iterations of a first-order predictor-corrector scheme (Ziegler, 2013a). Each trajectory from the individual radar

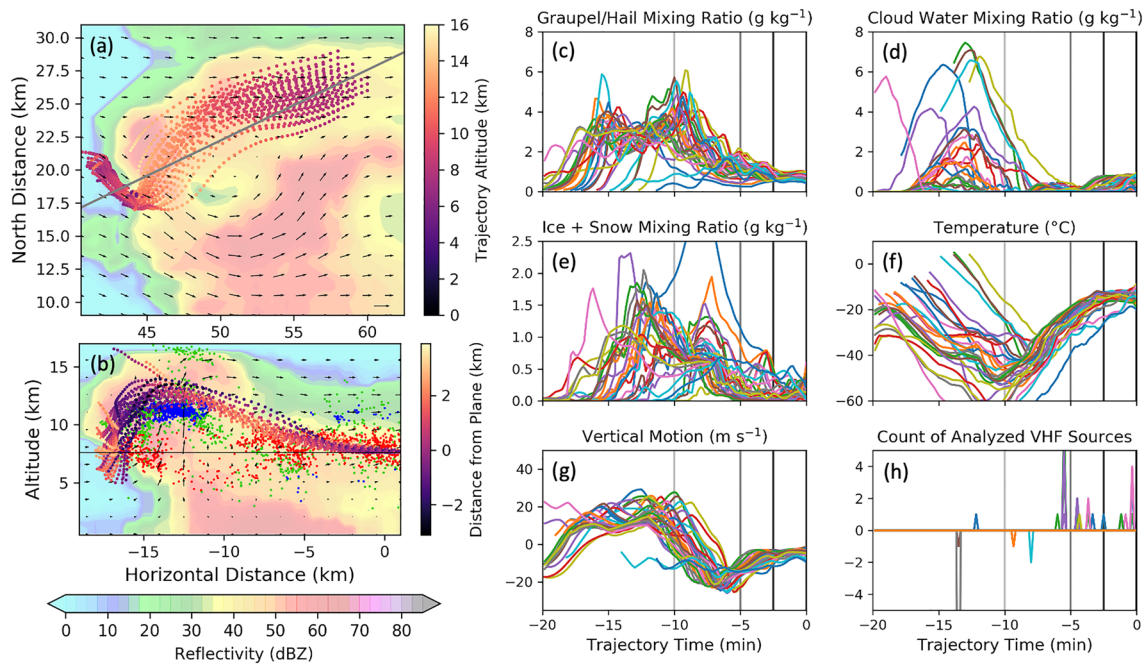


Figure 1. Conditions along backward-in-time graupel/hail trajectories that originated at the 7.575-km level in a $4 \times 4 \text{ km}^2$ (thinned to half the trajectories) at 2348 UTC until individual terminations as described in text. Left panels show storm-relative trajectory locations relative to reflectivity (dBZ) and winds (the 50 m s^{-1} horizontal vector is in the bottom right of both panels). (a) Horizontal cross section at an altitude of 7.575 km. Trajectory colors indicate altitude. The black horizontal line indicates the location of the vertical cross section in panel b. (b) Vertical cross section along the black line in panel a. Trajectory color indicates horizontal distance of the trajectory from the vertical plane in which negative values are to the southeast of the plane. The black line is the altitude of panel a. Red (blue and green) dots indicate VHF sources inferred to be positive (negative and undetermined) storm charge from 2348 to 2351 UTC and within 2 km of the vertical plane. Right columns indicate conditions along the graupel/hail trajectories: (c) graupel/hail mixing ratio, (d) cloud water mixing ratio, (e) ice plus snow mixing ratio, (f) temperature, (g) vertical speed of graupel/hail, and (h) VHF counts along each trajectory, positive (negative) for VHF sources in positive (negative) charge. Vertical lines demarcate 2.5-, 5-, 10-min histories for reference.

analysis times is followed backward in time for a maximum of either 20 min or else until an ambient local threshold minimum mixing ratio value chosen to represent embryonic precipitation particle formation has been achieved. The assumed minimum mixing ratio for graupel/hail trajectory initiation is 0.1 g kg^{-1} (e.g., as demonstrated in Figure 1c), while the assumed minimum mixing ratio for both ice or snow trajectory initiation is 0.05 g kg^{-1} . These mixing ratio formation threshold values are approximately 1% of their respective maximum diagnosed precipitation values in the storm.

Cloud environmental properties and hydrometeor characteristics within the trajectory time steps between the individual radar analyses times are calculated using trilinear spatial interpolation from the storm-motion advected radar fields following Ziegler (2013a). The hydrometeor and temperature fields are derived from the DLA (e.g., Figures 1c–1f). The sum of charge-analyzed VHF sources in a grid cell containing each backward trajectory within 10-s windows centered on each time step is recorded to represent the lightning-producing regions with identified charge that these trajectories traversed (Figure 1h), with the understanding that the VHF-centered analysis is likely under representing positive breakdown. Since the VHF likely also underrepresents the spatial extent of net charge, the full breadth of area contributing to breakdown could alternatively be better represented by flash extent density.

Locally small wind field variations may accumulate via 3-D airflow deformation to produce arbitrarily large local differences of Lagrangian parcel properties among the paths of neighboring graupel/hail trajectories. For example, the 8 g kg^{-1} spread of cloud water mixing ratio experienced by graupel/hail ascending through the updraft in different locations and times (Figure 1d) is caused by widely differing inflow parcel source levels and associated differences in local updraft lifting and inflow parcel potential temperature, vapor mixing ratio, relative humidity, and saturation point. At the given analysis time, however, all parcels reside within the same net-positive charge layer (Figure 1b). Therefore, all trajectory properties at prior times will be analyzed using the average of the trajectories terminating in neighboring grid cells, specifically within a

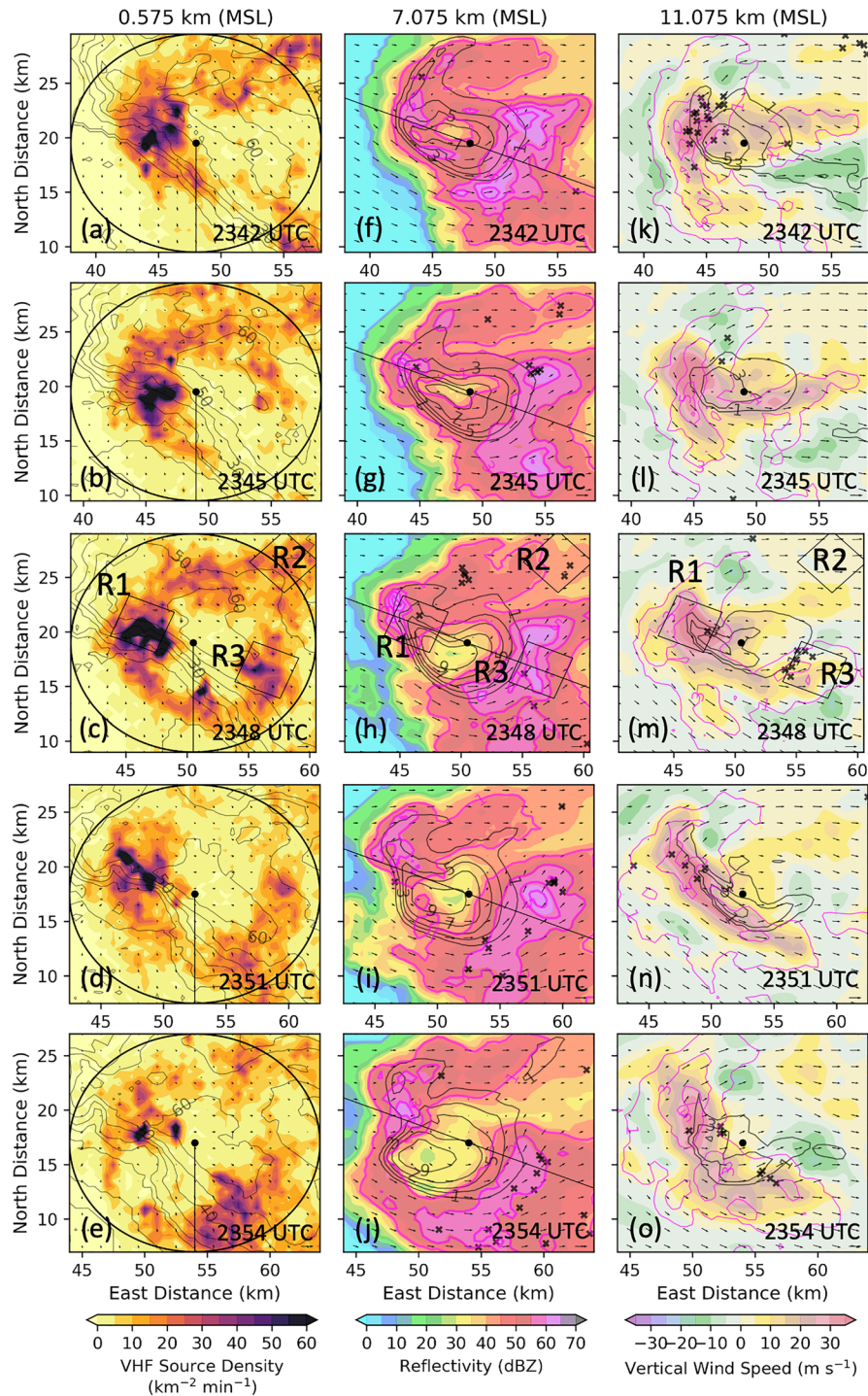


Figure 2. Overview of updraft region from 2342–2354 UTC (top to bottom) with horizontal wind vectors (the bottom right vector in each panel represents 50 m s^{-1}), flash centroids (“x”) within 1 min (e.g., 2342–2343 UTC), and 1 km of each level. Dot at reference center point in each panel. (a–e) Reflectivity at 0.575 km altitude (dBZ; contours in 10 dBZ increments from 10 dBZ) and average VHF density through the whole depth of the storm over the following 3 min (e.g., 2342–2345 UTC). The 10-km circle limits the analysis shown in Figure 3 in which the azimuths progress clockwise from marked radial at -180° to 180° from north. (f–j) Reflectivity (dBZ; filled), gaupel/hail mixing ratio (pink contours), and cloud water (black contours) at 1, 3, 5, 7, and 9 g kg^{-1} each at 7.075 km altitude. Slanted black line indicates the cross section shown in Figure 4. (k–o) Vertical wind speed (m s^{-1} ; filled), gaupel/hail (pink contours), and cloud water (black contours) mixing ratios at 1, 3, and 5 g kg^{-1} each at 11.075 km altitude. Regions R1–R3 are highlighted at 2348 UTC.

4×4 km area at each analysis level, to describe the characteristic environments experienced by hydrometeors on the scale of an analyzed charge region and lightning flashes. In the example of Figure 1, the trajectories terminating at the 7.757-km level at 2348 UTC averaged cloud water mixing ratios greater than 1 g kg^{-1} at 2338 UTC or 10 min prior and less than 0.5 g kg^{-1} at 5 and 2.5 min prior, the times shown by the vertical bars in Figure 1d. Each 4×4 km column was objectively centered on the maximum flash extent density at an angle of identified interest from a reference point (shown in the following section).

3. Observations

3.1. Overview and Temporal Variations

As described by DiGangi et al. (2016), the Kingfisher storm began to exhibit supercellular characteristics including low-level rotation at 2329 UTC after the initial formation of a bounded, relatively lightning-free localized subregion within the middle and upper levels of the main storm precipitation core at 2321 UTC (similar to Figures 2c–2e). This localized lightning-free region is here referred to as the “Bounded Weak Lightning Region” (BWL) following Ziegler et al. (2014), as the BWL is often capped by a mantle structure of high flash rates or small VHF events. The BWL terminology also conveniently corresponds to the analogous Bounded Weak Echo Region (BWER) that commonly describes a region of small precipitation content and weak radar reflectivity that typifies the intense midlevel updraft and precipitation cores of strong convective storms (e.g., Figures 2h–2j). The BWL structure has previously been identified by the existence of either a “lightning hole” (e.g., Krehbiel et al., 2000; MacGorman et al., 2005) or a contiguous midlevel “lightning ring” (Payne et al., 2010) that laterally bounds the lightning-free region (e.g., Figure 2c). The centroid of the BWL, BWER, and cloud water core were all consistently displaced somewhat downstream from the main updraft (e.g., Figures 2i and 2n). The lightning ring that laterally bounded the BWL became more circular after 2330 UTC and eventually confined within a roughly 10 km radius by 2345 UTC (Figure 2b). The weak echo region and cloud water core at the 7.075-km level visibly increased in coverage between 2342 and 2348 UTC, as shown in Figures 2f–2h. The lightning-free region was again bounded on all sides as flashes by 2348 UTC occurred immediately downshear of the cloud water core coincident with updraft and graupel/hail containing volumes (Figures 2c, 2h, and 2m). This time period with a bounded lightning-free region will serve as the focus of the electrification analysis in close proximity to the BWER, as it portrays the existence of separated net charge regions throughout the periphery of the SLW core.

Within the relatively narrow band of VHF activity inside a radius of 10 km from the BWER core (Figures 2a–2e), variations of flash polarity occurred as a function of azimuth around the BWER and BWL. The analyzed charge regions and relative altitudes and azimuths of VHF sources are shown within a cylindrical section at a 10 km radius from the BWL center (Figure 3) to illustrate the accumulated VHF activity in this narrow band. Flashes between a net positive charge layer from 7.5–10 km and negative charge aloft, an inverted dipole structure, surrounded the majority of the BWL (e.g., Figure 3, R1), but a lower negative charge layer was present northeast of the BWL at 2348–2351 UTC (Figure 3, R2), and the inverse structure was present to the east-southeast at the same time (Figure 3, R3). Discussion in this section will center around these three subregions with variations in vertical charge structures (R1–R3; Figure 3), their meteorological context, and their temporal evolution. Later sections will focus on the histories of graupel/hail trajectories analyzed within each subregion at 2348 UTC, when these distinct charging regimes surrounded the BWL, in order to diagnose the fundamental characteristics of the in cloud environments and three-dimensional transport, which could have generated these unique structures.

3.1.1. Region 1

The local maxima in flash rates and VHF sources (R1; Figures 2a–2e) was embedded within the western flank of the midlevel BWER and local maxima in cloud-water mixing ratio (Figures 2f–2j) and the lofting of significant graupel/hail and cloud water in strong updraft to upper levels (Figures 2k–2o). Temporally, the charge structure was relatively consistent, containing net positive charge at roughly 5–10 km and net negative charge at 10–12 km with dense VHF activity, an inverted dipole structure (Figure 3, area of R1). Occasional flashes during the 2342–2354 UTC period included positive breakdown into negative charge at 8–9 km, heights dominated by negative breakdown into positive charge without any spatial separation (e.g., Figure 3, 2342–2345 UTC at -100° to -50° from north), suggesting the presence of underrepresented pockets of negative charge amid the upper portion of the region dominated by positive charge. The upper-level structure characterized by -IC continued around the southern edge of the BWL with

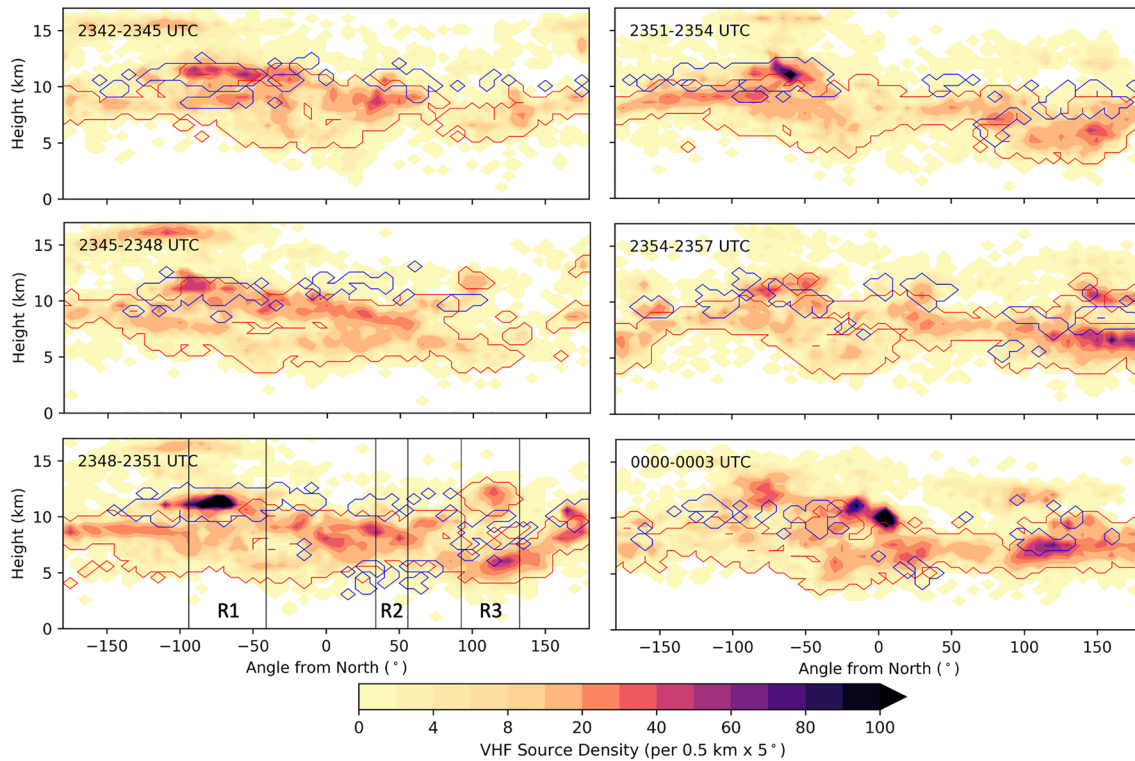


Figure 3. VHF sources summed in volumes each covering 3 min in time, 0.5 km in altitude, 5° in azimuth, and 0–10 km in radius volumes, as bounded by the 10-km radius circle shown in Figure 2, every 3 min from 2342–0000 UTC as labeled. Red and blue contours outline regions in which VHF sources were inferred to be associated with net positive and negative charge regions, respectively. Regions R1–R3 are highlighted at 2348–2351 UTC.

limited depths of positive charge (7.5–10 km; Figure 3, -180° to -90° from north) along the intersection of substantial cloud water and graupel/hail mixing ratios surrounding the 11.075-km layer (Figures 2k–2o). The uppermost altitudes surrounding the strong updraft also contained small VHF events in which no charge could be identified (note the unidentified VHF densities at 12–13 km and -80° from north from 0000–0003 UTC in Figure 3), which may suggest rapid charge replenishment at high altitudes and low breakdown thresholds but with locally insufficient wells of potential for flash propagation (e.g., Calhoun et al., 2013).

There was a substantial area of larger radar reflectivities at low levels to the northwest and upshear of R1 and the primary updraft owing to precipitation fallout (Figures 4a–4e). Winds of almost 20 m s^{-1} approached the updraft from the west throughout the precipitation curtain at 7–10 km (e.g., Figure 4a). Such inbound winds could ingest preexisting particles from the precipitation curtain including graupel/hail embryos into the updraft and promote graupel/hail production (as will be demonstrated in section 3.2.1), which in turn can participate in NI electrification. This process could have contributed to the locally enhanced flash rates, VHF densities (Figures 4a–4e) and radar returns (Figures 4f–4j) and thereby to the observed displacement in the BWER and BWLR from the updraft core (Figures 4f–4j). The strong winds would also force horizontal entrainment of dry environmental air through the upshear cloud edge, resulting in the lower temperatures and cloud liquid water contents resolved by the DLA along the southern and western edges of the updraft and reflectivity core (e.g., Figures 4e and 4j).

The positive charge in R1 was located on the outer edge of the 30 m s^{-1} updraft (Figures 4a–4e), where graupel/hail mixing ratios were maximized along the periphery of the SLW core (Figures 4f–4j). The positive charge was largely within temperatures warmer than -40°C (Figures 4a–4e), the level above which most cloud water is expected to convert to cloud ice via heterogeneous freezing, although graupel/hail was lofted much higher than the -40°C level due to the large net upward motions of vertically advected graupel/hail particles (Figures 4f–4j). The shallow layer containing positive leaders into negative charge extended inward toward the center of the BWER at the freezing level and above the SLW core (e.g., Figures 4c and 4d). This

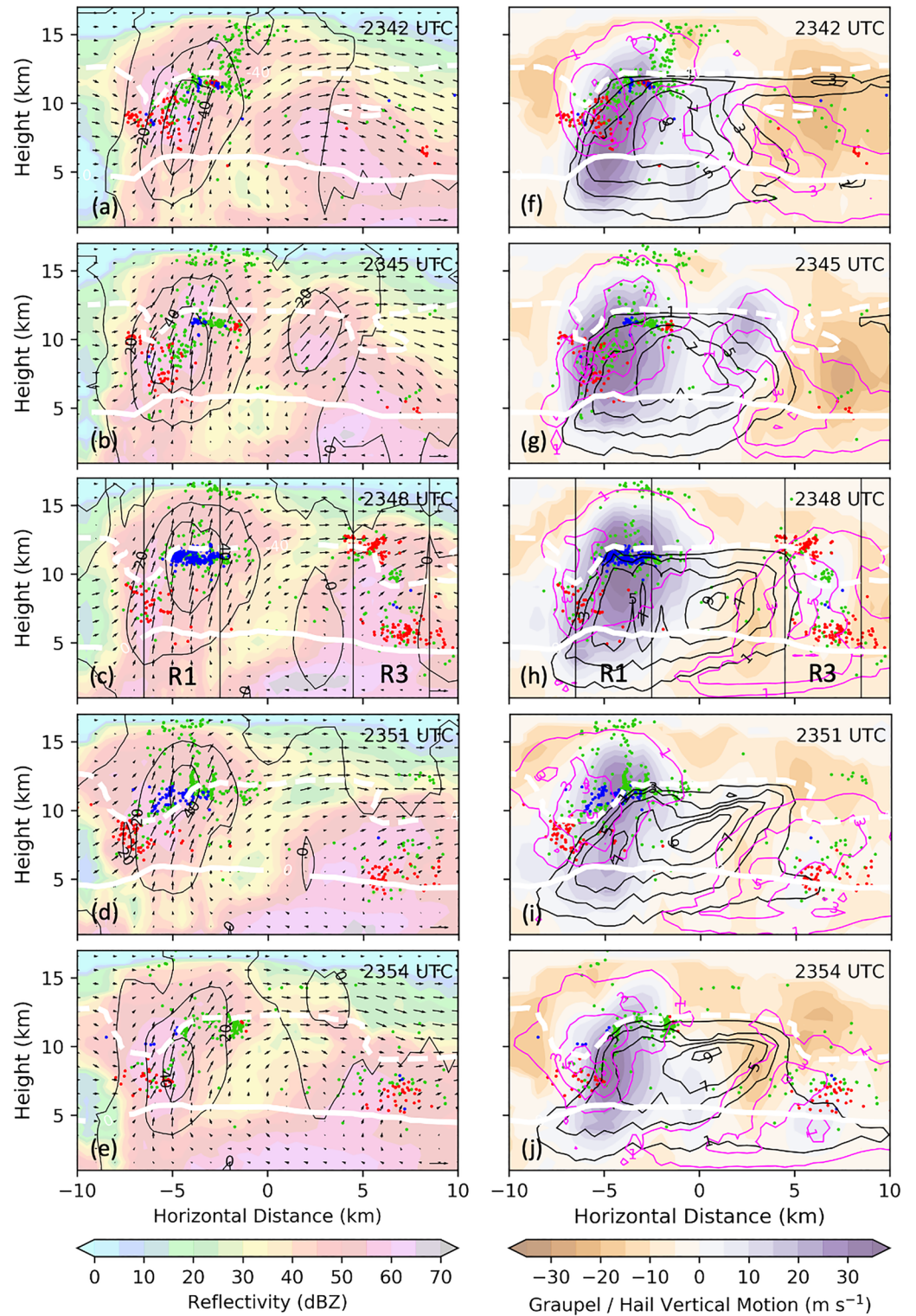


Figure 4. Vertical cross sections as indicated in Figures 2f–2j. (a–e) Vertical wind speed (contoured at 0, 20, and 40 m s^{-1}), vector winds along the plane (bottom right arrow is 50 m s^{-1}), reflectivity (shading; dBZ), and VHF sources (colored as in Figure 1) within 250 m of the plane over the following 3 min (e.g., 2342 UTC radar analysis includes VHF sources from 2342–2345 UTC). (f–j) Vertical velocity of mass-weighted graupel/hail ($w-v_T$; filled), graupel/hail mixing ratio (pink contours), and cloud water (black contours) at 1, 3, 5, 7, and 9 g kg^{-1} . White contours are 0°C (solid) and -40°C (dashed). Regions R1 and R3 are labeled at 2348 UTC.

horizontal displacement did not occur farther south. Although vigorous heterogeneous freezing of cloud droplets within the upper levels of the SLW core would produce abundant ice crystals for collisions with existing graupel/hail, simultaneously decreasing SLW would likely reduce local NI electrification rates above this level (e.g., Calhoun et al., 2014).

The persistent upper-level VHF sources associated with the overshooting top above 15 km on the western side of the BWLR over R1 during the 2342–2354 UTC period are noteworthy (Figure 3). These VHF sources were clustered along the 1 g kg^{-1} graupel/hail mixing ratio contour at the highest level in which graupel/hail was suspended during the 2345–2351 UTC period (Figures 4g–4i), indicating separation from the smaller cloud ice particles above the clustered high-altitude VHF source layer.

3.1.2. Region 2

A persistent band of VHF sources and flashes within R2 extending eastward from the northern periphery of the cloud water core into the forward flank (Figures 2a–2e) was unique in possessing a lower negative charge layer and an inverted tripole structure (Figure 3, 2348–2351 UTC). However, this persistent banded VHF source feature was not consistently present at other azimuths and time periods within 10 km of the BWLR. A transitional region between R1 and R2 was located north-northwest of the BWLR in the azimuth sector from -45° to 15° from north (e.g., Figure 3, 2348–2351 and 2354–2357 UTC), which contained a relative minimum in negative leaders propagating into positive charge around 8 km and positive leaders propagating into negative charge. This transitional region suggested the existence of a discontinuity in charge regions between R1 and R2 from either differential particle motion or varying electrification regimes.

A balloon-borne videonde and an electric field meter (EFM) sampled the anvil region roughly 5–10 km directly downstream from R2 (Waugh, 2016). The EFM measured a negative vertical field intensity of up to -80 kV m^{-1} at the base of the forward anvil precipitation layer (-15°C to -20°C) that transitioned to a positive vertical field of up to $+50 \text{ kV m}^{-1}$ within the anvil layer (-20°C to -27°C), suggesting a positive charge layer centered around -20°C . The latter EFM-observed vertical field profile of Waugh (2016) is internally consistent with an inverted tripole charge arrangement as inferred in the present study based on LMA-inferred flash polarity upstream.

3.1.3. Region 3

A vertically coherent updraft in R3 to the southeast and downshear of the BWER (Figure 4h) began producing comparable VHF densities to the other two regions at 2348 UTC (Figure 2c). This region differed from R1 or R2 in that its largest VHF densities (associated with positive charge) were at lower altitudes throughout the study period (5–8 km; Figure 3). There was also an elevated secondary VHF density maximum during the periods of 2348–2351 and 2354–2357 UTC that was associated with positive charge in the 10- to 13-km layer above the negative charge layer (Figure 3), resulting in a local charge structure within R3, which could be described as bottom-heavy normal tripole charge structure (e.g., Mansell et al., 2010). A similar structure present throughout a storm has also been described as anomalous due to the unusually large fraction of VHF activity in the lower layer of an otherwise normal tripole layering of net charge (e.g., Fuchs et al., 2015). Regardless, this local structure was significantly different than the charge structures surrounding the other sides of the BWER (e.g. Figure 3, R1 and R2). Although graupel/hail mixing ratios were consistently above 3 g kg^{-1} within R3, this subregion did not consistently participate in lightning flashes in other time periods (Figures 4f–4j). An updraft extended through the mixed-phase depths at 2348 UTC on the periphery of the liquid water core, either suspending or weakly lifting mass-weighted graupel/hail coincident with the column of VHF activity (Figure 4h), also shown in Figure 2m). In subsequent periods (Figures 3, 4d–4e, and 4i, and 4j) the updraft suspended graupel/hail mixing ratios in excess of 4 g kg^{-1} and VHF sources were confined to lower altitudes. However, the cloud water content increased locally near the melting level within this sustained low-level updraft (Figures 4i and 4j), potentially contributing to local electrification and sustained flashes in the following analysis times.

3.2. Graupel/Hail Histories

This section will detail the graupel/hail trajectories, and the characteristics along them likely to influence electrification, terminating within Subregions R1–R3 at 2348 UTC, when lightning surrounded the BWLR and the three distinctly different charge structures were present (e.g., Figure 5a). Subregion R1 and the mid-level positive charge wrapping around the southern side of the BWLR (Figures 5a and 5b) were dominated by lofted, recently formed graupel/hail (Figures 5c and 5d) as hypothesized that in turn implied the action of

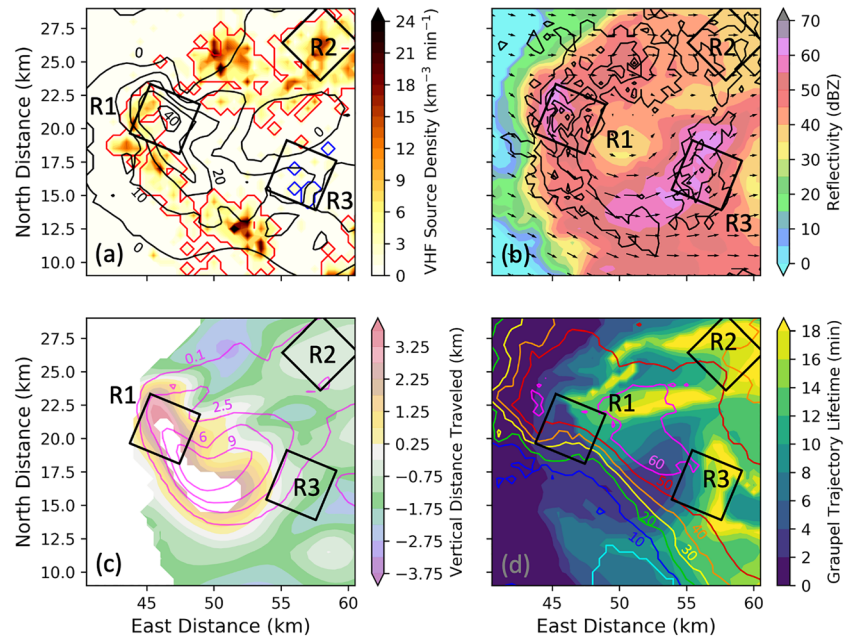


Figure 5. Lightning characteristics, radar reflectivity and winds, and retrieved microphysics at 2348–2351 UTC. Regions R1–R3 are labeled in each panel. (a) VHF source density at 7.825–8.325 km from 2348–2351 UTC (filled) and vertical wind speed (black contours; m s^{-1}) at 2348 UTC. Red and blue contours represent regions in which any VHF sources during the period were inferred to occur in net positive and negative charge regions, respectively. (b) Reflectivity at 8.025 km and average flash extent density per minute in 0.5×0.5 km grid cells from 2348–2351 UTC. (c) Vertical distance traveled by mass-weighted graupel/hail (filled) and maximum cloud water mixing ratio experienced (pink contours) at 0.1, 2.5, 6, and 9 g kg^{-1} over previous 2.5 min (234530 to 234800 UTC; empty volumes are either more nascent or absent graupel/hail). (d) Total lifetime of mass-weighted graupel/hail trajectories prior to 2348 UTC at 8.025 km (filled), lowest-level reflectivity (dBZ, contoured).

recent, local electrification, as would be expected near the updraft core. The midlevel positive charge to within R2 contained much longer-lived graupel/hail, which had been followed for up to 20 min (i.e., the maximum time period analyzed; Figure 5b) and which had experienced riming growth during the past 2.5 min (Figure 5c). Although Subregion R3, which contained midlevel negative charge (Figure 5a), also contained long-duration graupel/hail trajectories (Figure 5d), it nevertheless resided along the periphery of volumes capable of supporting recent graupel/hail riming growth (Figure 5c).

3.2.1. Region 1

As suggested by the combined radar analysis fields (Figures 2h and 4c), the initiations of many mass-weighted graupel/hail trajectories throughout the midlevels that terminated in R1 at both 7.575 and 11.075 km appear to have associated with embryonic snow particles entering the updraft from the upshear direction (Figure 6). Additional trajectories that terminated in the eastern portion of R1 at 5.075, 7.575, and 11.075 km traced their formation south of R1 (Figure 6) to an area of recycling, partially melted graupel/hail, and raindrops associated with moderate reflectivities around the melting level within the low-level southerly inflow (as demonstrated at the lowest level in Figures 2a–2f) in addition to the recently, locally generated graupel/hail in this regions (Figures 5c and 6). There was significant variation within the region as a combination of the horizontal variations (Figure 4h) and variable trajectories paths (Figure 6) and lifetimes (Figure S1a, 5c, and 5d) resulting in relatively large standard deviations (Figure S1). This discussion will focus on the average properties within the column as the net charge regions occur over a large area, with the understanding that individual trajectories may differ and promote opposing charge generation that may or may not be realized on the scale of the observed flashes.

The 3-D column comprising R1 contained the representative positive charge from the melting level to 10 km and negative charge from 10–12 km with much of the peak in negative VHF sources extending above the average height of -40°C (Figure 7a). Since graupel/hail had been lofted by deep updrafts exceeding

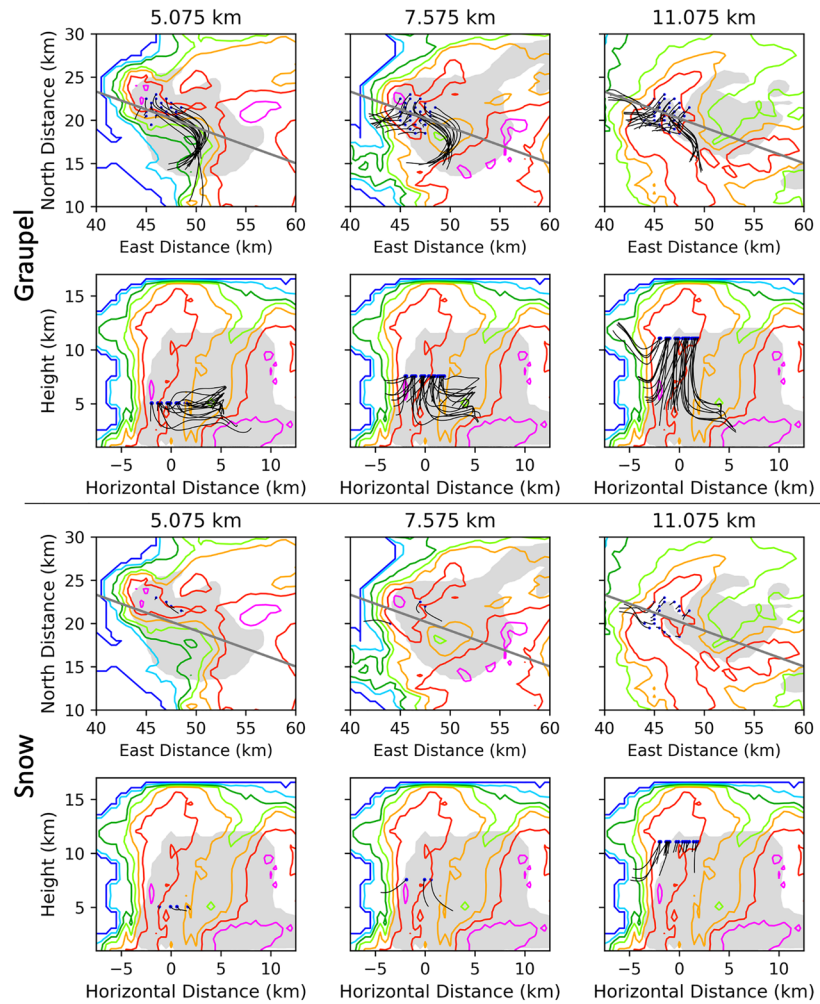


Figure 6. Storm-relative snow (lower panels) and mass-weighted graupel/hail (upper panels) trajectories that terminated at three altitudes (5.075, 7.575, or 11.075 km MSL) in R1 at 2348 UTC, superimposed on 2348 UTC reflectivity contours (dBZ, in 10 dBZ increments from 0 to 60 dBZ) and cloud water mixing ratio above 0.1 g kg^{-1} (gray fill) along horizontal and vertical planes at trajectory termination for reference. Gray lines in horizontal planes are the location of the corresponding vertical cross sections. Trajectories extend backward in time 20 min or until the minimum criteria for each particle type was met (0.1 and 0.05 g kg^{-1} for graupel/hail and snow, respectively). The lack of a trajectory ending at a particular location means that the mixing ratio was less than the given threshold at 2348 UTC.

30 m s^{-1} (Figures 4c, 4h, and 7b), the graupel/hail trajectories that terminated within the negative charge in the 10- to 12-km layer at 0048 UTC and had existed previously traveled through locations containing mainly positive VHF sources only 2.5 min earlier (Figure 7a). Given the horizontal displacement of these charge regions (Figure 4c) as well as the averaging of trajectories from across the whole area of R1 at this height, some graupel/hail could conceivably have traversed through only one charge layer. Interestingly, the -40°C homogeneous freezing level roughly coincided with the transition from increasing to decreasing ascent rates of graupel/hail trajectories over the previous 2.5 min (Figure 7b), suggesting vertical flux convergence of fast-falling graupel/hail particles near the negative VHF source maxima. It is also unexpected that the number of VHF sources analyzed to represent positive breakdown into negative charge within this column would be more numerous than into positive charge (Figure 7a), as the VHF emissions within positive charge are typically more numerous. This unusual bias within the column total is likely caused by both the negative charge layer being shallower than the positive charge layer and the flash channels within the positive charge layer propagating outside of the column boundary (Figure 4c).

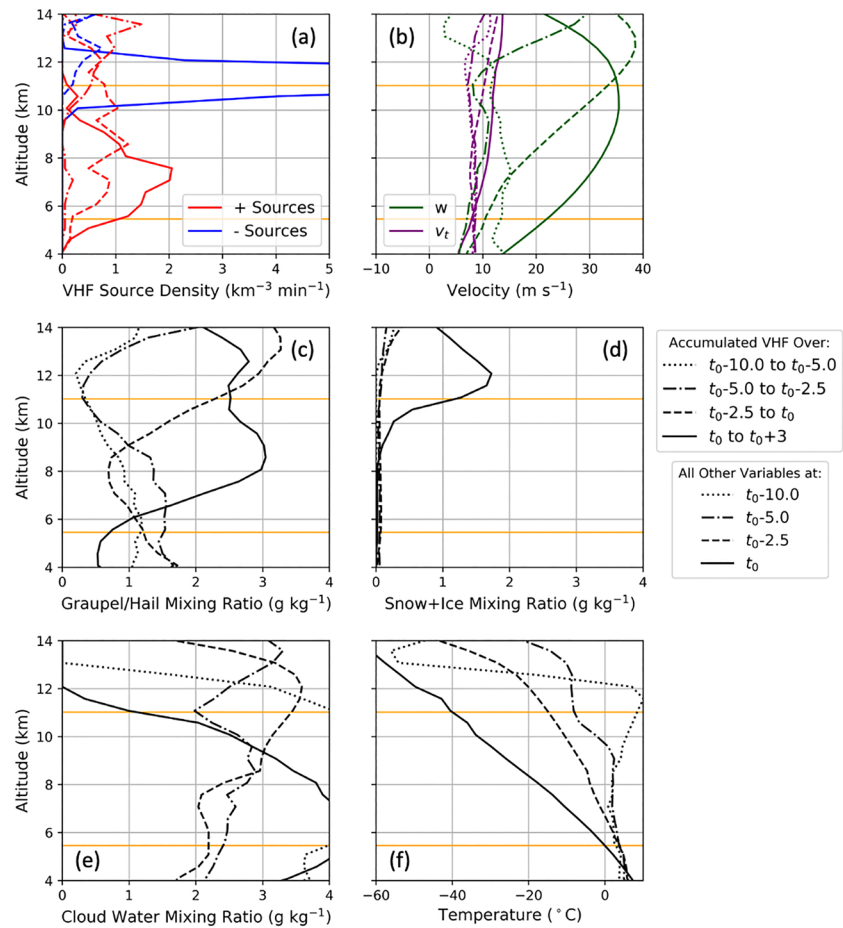


Figure 7. The average value of various properties along mass-weighted graupel/hail trajectories terminating at each height in Column R1 at $t_0 = 2348$ UTC (including those in Figure 6; see Figure 1) at each of four times (2338, 2343, 2345:30, and 2348 UTC or 10, 5, 2.5, and 0 min prior to t_0 in panels b–f) or time periods (2338–2343, 2343:00–2345:30, 2345:30–2348:00, and 2348–2351 UTC in panel a), to sample the evolution along trajectories ending in each layer. Note that the properties tracked at earlier times are plotted by terminal altitude not by the altitude of the trajectories at earlier times, which varied considerably from the terminal altitude. Missing contours indicate graupel/hail trajectories did not continue to the listed time. (a) VHF source density of sources analyzed to have been in positive charge (red) or negative charge (blue), normalized to $\text{km}^{-3} \text{min}^{-1}$. (b) Terminal fall speed (v_t) and vertical wind speed (w), mixing ratios of (c) graupel/hail ($q_{g,h}$), (d) combined snow and ice ($q_{s,i}$), and (e) cloud droplets (q_c ; g kg^{-1}) and (f) temperature. Orange horizontal lines indicate the average altitude of 0°C and -40°C in R1 at t_0 .

Graupel/hail mixing ratios grew rapidly within the storm updraft (Figure 7c) via riming in significant SLW content within the previous 2.5 min (Figure 7e) coincident with increasing positive charge (Figure 7a), suggesting recent electrification. Graupel/hail mixing ratios following mass-weighted trajectories that terminated between 8 and 9 km increased by more than 2 g kg^{-1} in 2.5 min and exceeded 3 g kg^{-1} by 0048 UTC (Figure 7c; standard deviations shown in Figure S1). Although the *mean* inferred snow and cloud ice mixing ratios following the graupel/hail trajectories below 8 km were relatively small (Figure 7d) with likewise small standard deviations (Figure S1), they are more than adequate to associate with the relatively large total ice particle concentrations. Significant snow and cloud ice concentrations supporting NI electrification did exist along some individual trajectories (up to $4.5 \times 10^3 \text{ m}^{-3}$ and $3.7 \times 10^7 \text{ m}^{-3}$ in the previous minute of graupel/hail trajectories terminating at 8.075 km, respectively). Graupel/hail was likely the positive charge carrier since abundant SLW (Figure 7e) can favor positive rimer electrification. In addition, temperatures along the graupel/hail trajectories earlier during their evolution were warmer than -20°C (Figure 7f), also favoring positive graupel/hail electrification. It is intriguing that this deep positive layer overlapped a region in which graupel embryos were entrained from the west into a region of plentiful SLW (Figures 4c and 4h),

thereby providing a third factor supporting particle interactions producing positive charge on graupel/hail particles to supplement positive charges on graupel/hail particles ingested via low-level inflow. This westward source of rapidly growing graupel may have contributed also to the noted offset of the BWER from the core of the strongest updrafts.

The SLW encountered by ascending graupel/hail particles above 9 km decreased rapidly from at least 3 g kg^{-1} to less than 1 g kg^{-1} on average by 11 km and the -40°C level and was effectively zero by 12 km (Figure 7e) where the mass-weighted graupel/hail experienced the most substantial temperature decrease over the previous 10 min (Figure 7d). Snow and ice mixing ratios increased rapidly as SLW decreased (Figures 7e and 7d) with these rapidly cooling temperatures (Figure 7f), suggesting that graupel/hail particles may have had opportunity to charge negatively in rebounding collisions with the rapidly forming snow and cloud ice particles. Thus, the negative charge layer above 10 km likely was due to a combination of rising negatively charged snow and cloud ice particles from lower levels generated in the previous 2.5 to 5 min and negatively charged graupel from more recent interactions at these lower temperatures.

Previous research developed the hypothesis that an inverted net space charge structure in the updraft core forms via positively charged graupel/hail at lower to middle levels and negatively charge ice particles at upper levels (e.g., MacGorman et al., 2008, 2011), one extreme of the continuum of NI electrification structures possible from variations in the updraft environment (Bruning et al., 2014). The updraft core is emphasized, as it can be the most pure representation of NI charge separation before complex motions contribute to the arrangement of complicated charge layers in other portions of the storm (e.g., Stolzenburg et al., 1998; Wiens et al., 2005). Even so, it may be too simplistic a conceptual model to apply to even R1, the subset region containing the main updraft core. The extension of the negative charge layer was displaced from the positive charge near the deep updraft (Figures 4c and 4h). Rapidly nucleated, vigorously riming graupel/hail (Figures 7c and 7e) from reingested ice particle embryos (Figure 6) likely charged positively through the depth of the SLW-containing main updraft core (Figures 7a, 7d, and 7e). In the narrow layer, which extends inward over the BWER and in which graupel/hail converged vertically (Figures 7a and 7b) while experiencing rapidly decreasing SLW due to heterogeneous freezing (Figures 7d and 7e), they likely experienced net negative NI electrification, as would be supported by both the low SLW content and temperatures (Figures 7e and 7f). Furthermore, rapid horizontal transport at greater than 20 m s^{-1} by the diverging winds above 12 km (Figure 7c) may have limited the spatial accumulation of charged cloud ice particles above that level. This potential charging pattern in R1 would be somewhat opposite but complementary to that described by Wiens et al. (2005), in which the majority of graupel in the updraft core was hypothesized to electrify positively due to the large SLW content while more graupel on the periphery of the updraft core was hypothesized to electrify negatively due to limited SLW. While the hypotheses here at first seem contradictory to those of Wiens et al. (2005), together, they describe a continuum of possible NI graupel/hail and smaller ice electrification volumes within a storm core in which either extreme might be minimized—the outermost updraft volume might not contain sufficient hydrometeors for efficient electrification, and the innermost might not contain enough rebounding particle interactions due to the high SLW content if the vertical convergence were not colocated with homogeneous freezing and mixed-phase particles.

It is, of course, likely that the charge regions of R1 are more complicated than can be illustrated by VHF analysis. The aforementioned individual flashes, which initiated at heights that would not be expected to have large electric field magnitudes based on the overall inferred charge regions, suggest a more complicated charge distribution than is revealed by the flash and therefore time-integrated analysis described above. This could be from some small variations in particle electrification due to local variations in environment or particle types (e.g., Avila et al., 2005; Glassmeier et al., 2018; Tsenova & Mitzeva, 2009) or even from likely charge deposited by flashes on ice particles within this region of high flash rates as hypothesized by MacGorman and Burgess (1994) and as simulated by Helsdon et al. (1992). As this region did also contain small events that could not be analyzed as previously mentioned, it is likely that there was at least rapid charge replenishment and perhaps small-scale heterogeneities in electrification regimes.

3.2.2. Region 2

The majority of mass-weighted graupel/hail particles on the northeast BWER flank within R2 at 5.075 and 7.575 km were lofted through the deep updraft before being ejected on the northern side of the circulation (Figure 8), traveling through the same region that produced the graupel/hail within the negative charge

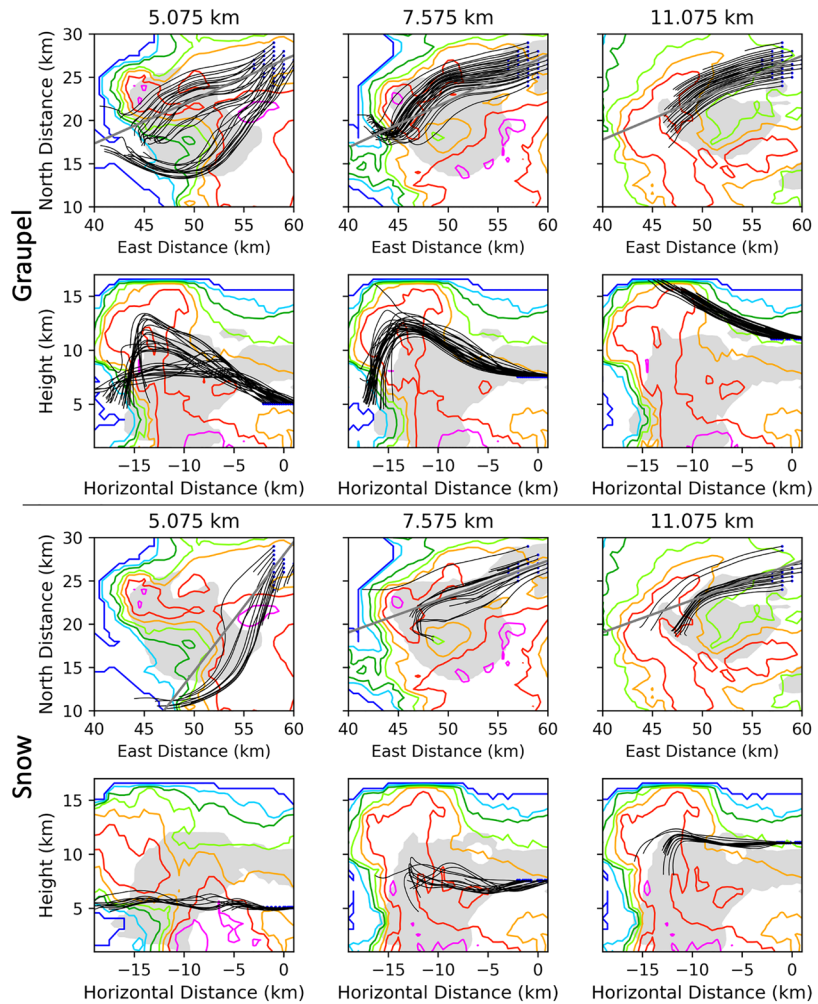


Figure 8. As in Figure 6 but for R2.

layer of R1 roughly ten minutes prior (Figures 9a–9c and S2). Some graupel/hail particles at lower levels including 5.075 km in R2 also came from trajectories that wrapped cyclonically around the BWER (Figure 8). Mass-weighted graupel/hail trajectories terminating in the upper region of R2 around 11.075 km originated from embryonic snow particles near the overshooting top (Figure 8) and relatively little diversity in recent trajectory environments (Figure S2) compared to R1 (Figure S1). The horizontal paths of mass-weighted snow were similar to that of some graupel/hail trajectories, although slow-falling snow particles generally originated outside regions of strong updraft and thus had less change in elevation along their paths (Figure 8).

The aforementioned balloon-borne videosonde and EFM profiles of the left-forward anvil precipitation region (Waugh, 2016; Waugh et al., 2018) provide precipitation measurements to help validate the present DLA-derived computed bulk graupel/hail and snow particle trajectories that pass through R2. The videosonde observations (immediately downstream from R2) reveal significant concentrations of ~2–4 mm diameter graupel and irregular snow particles with much larger concentrations of smaller (~0.6–2 mm) snow particles (Waugh et al., 2018), thus providing independent confirmation of the presence of the DLA-derived graupel/hail and snow particles in the left-forward anvil.

The R2 column had VHF sources in positive charge in the 6- to 10-km layer (-7°C to -27°C) and negative charge at both 10–12 km (just below the -40°C level) and around 4–6 km (just above the 0°C level; Figure 9a) on the northeast flank of the BWER during the period of 2348–2351 UTC (Figure 5a). The VHF source densities within the inferred negative charge layers were much smaller than those in positive

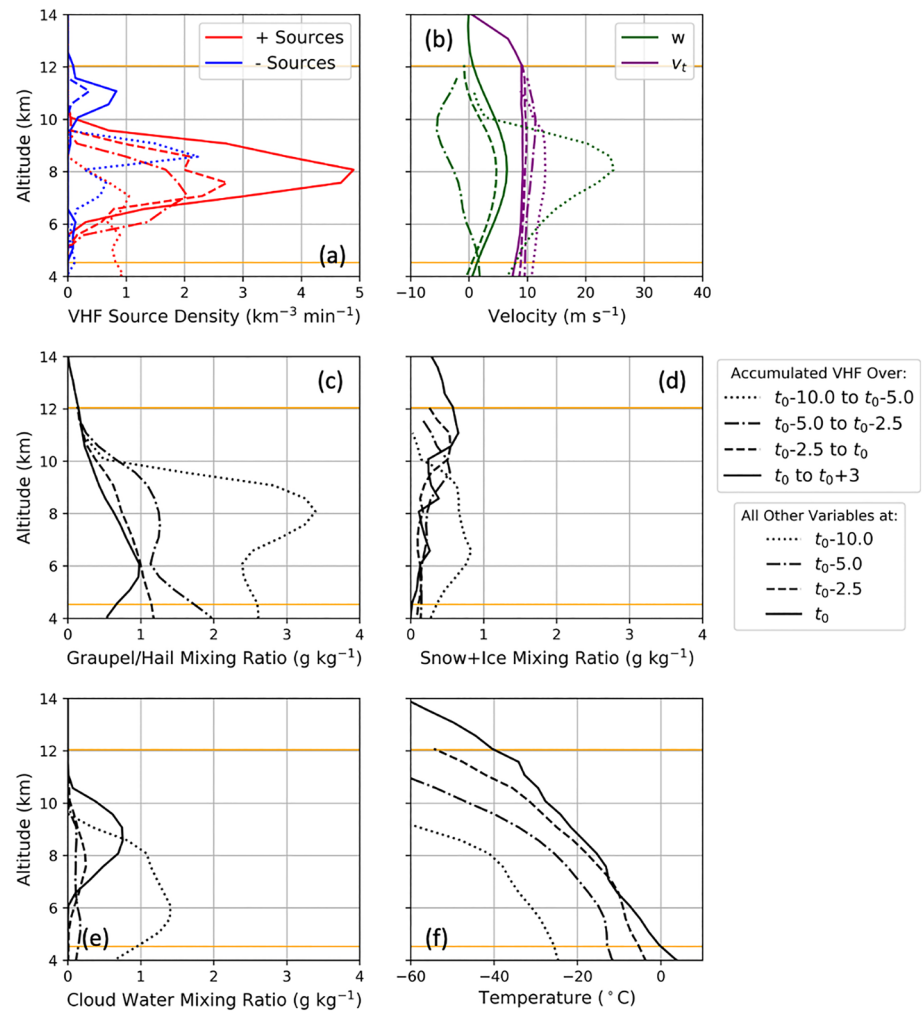


Figure 9. As in Figure 7 but for R2.

charge (Figure 9a), consistent with known VHF mapping system biases. Net upward wind speeds less than 10 m s^{-1} were present in the 4.5–12 km MSL layer throughout the depth supporting mixed-phase precipitation beginning at 2343 UTC (5 min prior to the analysis; Figure 9b). This net upward wind speed was insufficient to suspend mass-weighted graupel/hail anywhere in the column (Figure 9b). However, it was sufficient to provide modest SLW content at 2348 UTC of less than 1 g kg^{-1} in the 6- to 10.5-km layer (-7°C to -29°C ; Figures 9e and 9f). The graupel/hail trajectories which in this layer of R2 passed through regions with existing but limited SLW content (Figure 9e) in the previous 5 min as the trajectories slowly descended (Figures 8 and 9b) and warmed (Figure 9f), reaching their recent maxima in both temperature and SLW at 2348 UTC. Previously, the graupel/hail trajectories had experienced faster updrafts and higher SLW content when they passed through the primary updraft 10 min prior (Figures 9b and 9e).

Graupel/hail mixing ratios following trajectories that terminated within R2 were typically less than 1 g kg^{-1} at 2348 UTC (Figure 9c) since those trajectories generally traversed the edge of the reflectivity core (Figure 8). Ice and snow particles accounted for most of the diagnosed hydrometeor mass above 10 km (Figure 9d), while graupel/hail mixing ratios predominated below 10 km (Figure 9c). Because these ranges correspond to the altitudes at which VHF sources were inferred to be within negative and positive charge regions (Figure 9a), respectively, the positive charge was likely carried following convection by graupel/hail while the negative charge was likely carried by cloud ice and snow. Note that graupel/hail in the net positive charge layer at 2348 UTC had previously passed through the primary updraft (Figure 9b).

Those in the upper two thirds of the net positive charge layer at 2348 UTC had a comparable or greater VHF source density associated with negative charge than associated with positive charge 5–10 min earlier (Figure 9a). Because the detection efficiency for VHF sources in negative charge is much smaller, this suggests there was a significant reversal after 2343 UTC in the charge along the graupel/hail trajectories terminating in R2. Two time periods along the trajectories contained the SLW favorable for NI electrification (e.g., Illingworth & Latham, 1977; Saunders & Peck, 1998; Takahashi, 1978). Perhaps the recent albeit limited SLW interaction (Figure 9e) during descent (Figure 9b) and increasing temperatures (Figure 9f) somehow enhanced the probability of local, positive graupel/hail electrification during collisions with the rising cloud ice and horizontally advected snow at midlevels (Figure 8) in the previous 5 min, or perhaps the charge was generated in and carried from the updraft at least 10 min prior with the negative charge more efficiently dissipated from particles at the top of the updraft.

To summarize the microphysical and electrical morphology of column R2, the persistent midlevel updraft and locally sustained SLW content was a consistent feature along the northern side of the BWER (Figure 5c) consistent with the large-scale transition in charge distributions (i.e., Figures 3 and 5a). Compared to the southern side of the BWER, the midlevel high reflectivity core and significant graupel/hail mixing ratios did not extend as far eastward, but VHF densities were often larger near the BWER (2342–2351 UTC in Figure 2; flash extent density in DiGangi et al., 2016), suggesting that net charge generation may have been more efficient on the northern storm flank even in the presence of smaller graupel/hail concentrations. Part of this discrepancy could be (1) the more consistent particle replenishment from the updraft with time for differential sedimentation, since many of these particles at midlevels passed through the updraft core while those on the southern flank included graupel/hail that originated in the precipitation curtain southwest of the BWER (as will be discussed in the following section); (2) the potential local enhancement of NI electrification in the broad, SLW-supporting updraft region on the northern flank, which was spatially limited on the southern flank (Figure 5c); and (3) the relatively larger depth of precipitation and charge carriers on the northern flank near the BWER (Figure 2), or some combination of such factors.

3.2.3. Region 3

The graupel/hail trajectories terminating on the southeastern periphery of the BWER and cloud water core in R3 (Figure 10) traced very different paths than those on the northern storm flank (Figure 8). Most graupel/hail and snow trajectories terminating at 5.075 and 7.575 km were advected cyclonically around the cloud water core and originated in the precipitation curtain southwest of the BWER (Figure 10). The portion of this cyclonically curved trajectory of graupel/hail and snow particles within the southern flank of the main updraft and cloud core was previously identified as a predominant midlevel riming growth trajectory by Heymsfield and Musil (1982) and Ziegler et al. (1983). Most graupel/hail trajectories that terminated at 11.075 km within R3 originated near the updraft core (Figure 10).

Region 3 contained a localized, bottom-heavy normal tripole charge structure (e.g., Mansell et al., 2010) with net positive charge from 4–7 km, negative charge from 7–10 km, and upper positive charge from 10–13 km (Figure 11a). As in R2, the VHF source densities within the negative charge layers were much less than those in positive charge. The column defined by R3 was significantly colder than either R1 or R2 (Figures 7a and 9a), as exemplified by its average -40°C level residing below 10 km (Figure 11f). As in R2, the graupel/hail trajectories typically descended in weak updrafts generally less than 10 m s^{-1} (Figure 11b). However, updrafts at 2348 UTC increased gradually with height through the depth of the mixed-phase region and achieved maximum values near the -40°C level for the previous 2.5 min (Figure 11b). Column R3 contained limited SLW up to 12 km (Figure 11e), although both spatial heterogeneity (Figure 4h) and the spread of graupel/hail trajectories (Figure 10) contributed to the preponderance of average trajectory-following SLW above the freezing level (see large upper-level variability in Figure S3). The graupel/hail mixing ratios increased at nearly all levels with time along the ensemble paths of the mass-weighted trajectory paths (Figure 11c) in agreement with a riming growth trajectory (e.g., Heymsfield & Musil, 1982; Ziegler et al., 1983).

Graupel/hail trajectories terminating in the lower charge region appeared to travel primarily through positive charge (Figure 11a), so graupel/hail particles may reasonably have carried charge from elsewhere in the storm following the trajectories shown in Figure 10 over at least the previous 5 min. Additionally, the falling graupel recently experienced temperatures warmer than -20°C (Figure 11f) within limited cloud water content (Figure 11e) with existing smaller ice and snow contents analyzed within the same levels (Figure 11d),

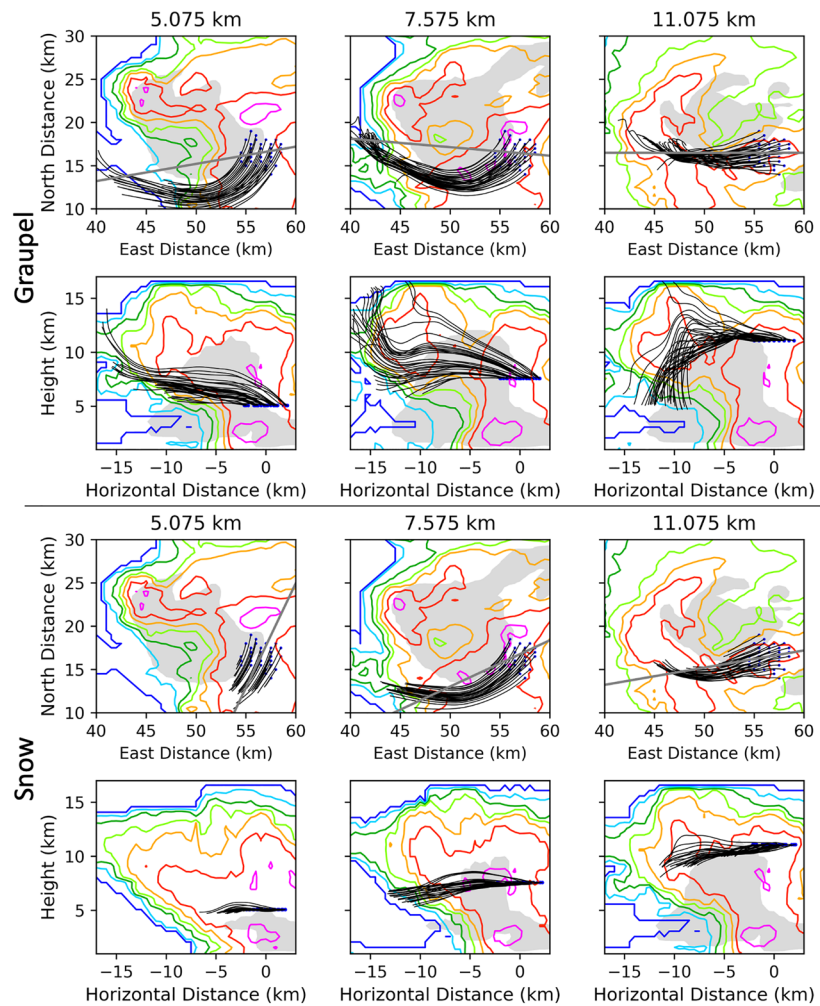


Figure 10. As in Figure 6 but for R3.

so additional collisions could further promote positive graupel (and negative ice) electrification due to the warmth of the lower layer (Figure 11f) in the most recent 0 to 2.5 min. Graupel/hail trajectories terminating in the other layers, however, passed through regions containing both charge polarities within the previous 10 min (Figure 11a).

Graupel/hail trajectories terminating within the 7.5- to 10-km layer dominated by net negative charge at 2348 UTC were also descending (Figure 11b) into warmer but still cold temperatures (-40°C to -25°C at 2348 UTC; Figure 11f) with limited cloud water (Figure 11e) and large snow and ice mixing ratios (Figure 11d) in the column. Given the relatively cold and dry conditions, NI electrification would be expected to produce negatively charged graupel/hail (and positively charged ice) in the negative layer in the previous 5 min. Cloud ice was likely still rising as indicated by the analyzed updrafts (Figures 4c and 11b), which would produce negative charge in this layer as a combination of the negatively charged ice from the electrification layer below and the negatively charged graupel/hail from this region. The past VHF inferred charge along the graupel/hail trajectories was mixed (Figure 11a), which may suggest nascent charge separation in this layer or may simply be a byproduct of the spread of trajectories, which terminated in this charge region (Figure S3). Regardless, it is worth noting that some of the mass-weighted graupel/hail trajectories terminating within the low-level negative charge layer in R2 passed through R3 previously at the altitude of the negative charge layer (Figure 8), so any negative graupel electrification in R3 also helps explain the existence of low-level negative charge layer in R2, supporting the hypothesis of how downshear charge structures may be organized presented by Wiens et al. (2005).

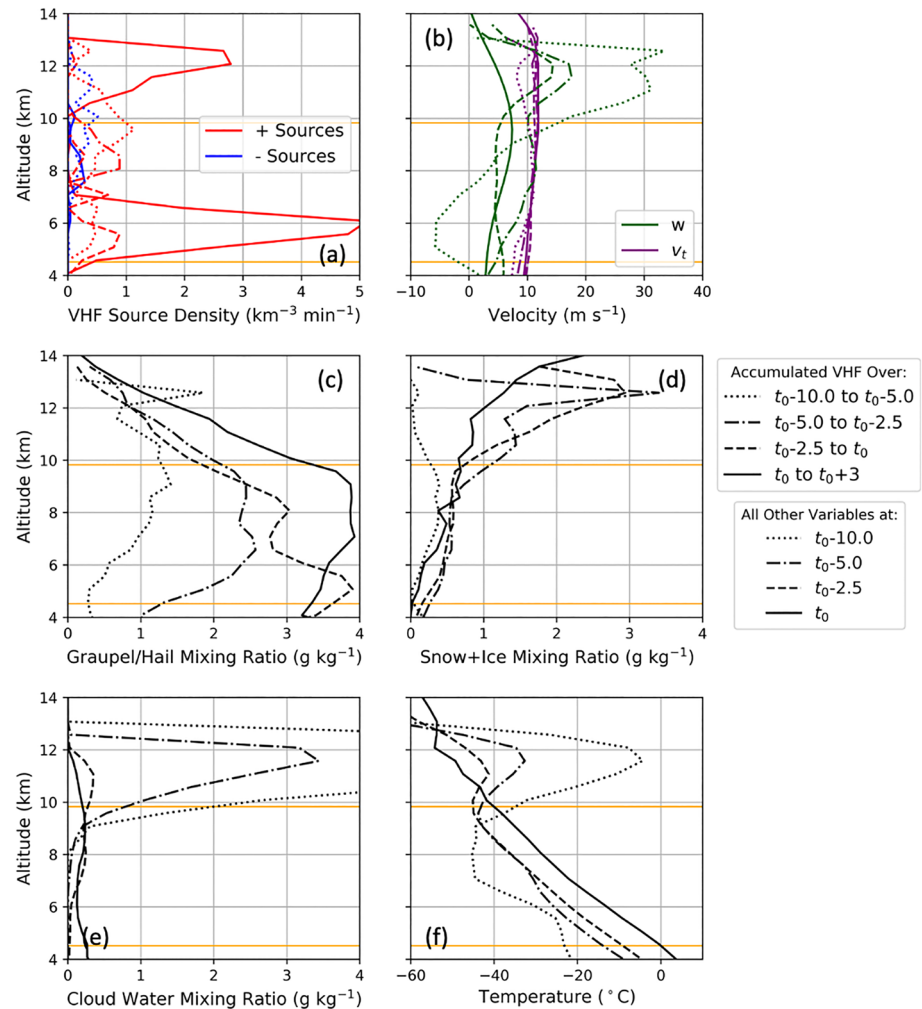


Figure 11. As in Figure 7 but for R3.

The positive charge above 10 km is at or colder than the -40°C isotherm (Figure 11a) and consists of graupel/hail trajectories that had risen through and subsequently detrained and fallen from strong updraft (Figures 10 and 11b) combined with relatively large mixing ratios of snow and ice, which have been advected around the BWER (Figures 10 and 11d). Charge carried on any single particle type cannot be shown with this data set, but positively charged ice particles would be expected at upper levels from recent collisions with graupel/hail contributing to negative charge in the 7.5- to 10-km layer. However, graupel/hail was still a major component of total precipitation content in this layer, as evidenced by values of reflectivity were ≥ 40 dBZ (Figures 4 and 11c). Graupel/hail trajectories had passed through much warmer environment (Figure 11f) with more SLW within the updraft 10 min prior to 2348 UTC (Figure 11e), which may have created positively charged graupel/hail and enhanced positive charge already carried in this area on ice generated more locally. However, the graupel/hail trajectories 5 min earlier were in a much colder environment where the opposite electrification might reasonably be expected (Figure 11f). Although this likely explains the mixed VHF sources along the trajectories 5 to 10 min earlier (Figure 11a), it remains unclear whether graupel/hail contributed to this upper positive charge layer.

4. Discussion and Conclusions

The initial analysis of the 29–30 May 2012 supercell storm near Kingfisher, Oklahoma, observed during the Deep Convective Clouds and Chemistry (DC3) field program (DiGangi et al., 2016) found that the vertical

polarity of the overall charge distribution inferred from the OKLMA was anomalous, with positive charge at altitudes usually containing negative charge and negative charge at altitudes usually containing positive charge. The current study presents a more detailed analysis focusing on lightning in three concurrent regions near the mesocyclonic updraft. Although two of the regions near the updraft (R1 and R2) did have traditional anomalous vertical charge distributions (an inverted dipole and an inverted tripole, respectively; Figures 3, 4, 7, and 9), the vertical charge distribution in one region near the updraft (R3) had a relatively normal tripole structure (Figures 3, 4, and 11).

To elucidate why charge distributions with both anomalous and normal polarities were present near the updraft core, we applied a DLA (DiGangi et al., 2016; Ziegler, 2013a, 2013b) to the evolving four-dimensional wind and reflectivity fields observed by multiple Doppler radars from 2251 to 0000 UTC, to estimate potential temperature and mixing ratios of cloud water, rain, snow, cloud ice, combined graupel and hail (graupel/hail), and water vapor. We examined mass-weighted snow and graupel/hail trajectories that terminated at grid points throughout a $4\text{ km} \times 4\text{ km}$ column in each of the three regions that had strikingly different charge structures at 2348 UTC (Figures 6, 8, and 10). These trajectories provided information on the history of in-cloud environmental factors expected to influence NI charging following graupel/hail (Figures 7, 9, and 11).

All of the regions with flashes near the core of the updraft shared some common characteristics. All were in regions with updraft throughout at least a 7-km column and exceeding 5 m s^{-1} at some level within the layer supporting mixed-phase precipitation. They were on the periphery of the liquid water core and contained at least 2 g kg^{-1} graupel/hail, supportive of local NI electrification given the adequate smaller ice concentrations in such mixed-phase conditions—in each region the graupel/hail trajectories terminating at 8.075 km interacted with up to $4.5 \cdot 10^3\text{ m}^{-3}$ snow particles in the minute prior to the 2348 UTC analysis, roughly three times the concentrations of snow particles in Ziegler et al. (1986), and even more cloud ice particles ranging from $1.1 \cdot 10^7\text{ m}^{-3}$ in R2 to $3.7 \cdot 10^7\text{ m}^{-3}$ in R1, which is still an order of magnitude smaller than the maxima of cloud ice particles in Ziegler et al. (1986).

Local variations in environment around the updraft core of the Kingfisher storm seem important to the storm's anomalous electrification via perhaps nonintuitive scenarios. Anomalous charge structures were not restricted to regions with the fastest updrafts (e.g., Fuchs et al., 2015; MacGorman et al., 2005, 2017) with little recirculation of ice particles to scavenge SLW in the mixed-phase region (MacGorman et al., 2005, 2011). In fact, anomalous Regions R1 and R2 both contained ingestion of preexisting ice particles into SLW-containing volumes of the storm. Perhaps, if such scavenging occurred through more of the storm depth and updraft area, the broad area of SLW supply has been depleted by riming precipitation growth at warmer temperatures and resulted in different storm-scale electrification. It is important to keep in mind that the substorm-scale features discussed here may be common but not apparent in larger-scale studies correlating storm polarity to environmental properties (e.g., Carey & Buffalo, 2007; Fuchs et al., 2018) and overall storm characteristics (e.g., Fuchs et al., 2015). However, it seems to make sense that scavenging played a role in promoting the anomalous charge structures in this case by provided a sustained volume of rapid graupel growth on the periphery of and without depleting the SLW core. While the BWLR or lightning hole was coincident with the BWER and SLW core, as often observed in supercells (e.g., Calhoun et al., 2013; Krehbiel et al., 2000; MacGorman et al., 2005; Wiens et al., 2005), the strong inbound winds at midlevels complicated expectations (especially in R1) by ingesting snow and cloud ice on the periphery of the primary updraft (Figure 6). These particles then interacted with available cloud water (Figure 4), thereby enhancing local ice growth (Figure 7c), providing ideal conditions for NI electrification conditions and offsetting the centroids of both the SLW core and lightning hole from the core of strongest updraft (Figure 2; DiGangi et al., 2016).

As hypothesized by Wiens et al. (2005) and Bruning et al. (2014), not all vertical charge distributions resulted from graupel/hail and small cloud ice particles interacting and separating after rising together in an updraft, even near the updraft core, as other previous hypotheses assumed (e.g., Lang et al., 2004; MacGorman et al., 2005; Stolzenburg et al., 1998). Many of the graupel/hail trajectories terminating in regions east of the mesocyclonic updraft originated on the western side of the storm and traveled horizontally around the updraft (e.g., Figure 10), similar to the scenario for large hail growth both observed by Musil et al. (1986) and Lagrangian-modeled by Miller et al. (1988) in a High Plains supercell storm and Lagrangian-modeled by Ziegler et al. (1983) in an intense Oklahoma multicell storm. Furthermore, the snow that ended up in

these regions may have followed different trajectories than graupel. Thus, any charge separation from different particles in the same column could have been generated from separate interactions and microphysical conditions than are present within the final locations and resolved flashes.

The analysis in Figures 7, 9, and 11 tries to bound the uncertainty of the final issue by showing the microphysical conditions and charge experienced only by the mass-weighted graupel/hail particles at select times along the trajectories that terminated at each altitude. While this procedure provided hints as to why a particular polarity of charge may have been produced at a particular ending trajectory, one must keep the necessary limitations of this procedure in mind when interpreting the results, limitations that are similar to those involved in comparing electrified storm simulations with observed behaviors (e.g., Mansell et al., 2005, 2010)

- The analyzed charges were inferred from a VHF lightning mapping system, not the actual ambient charge, which provides no information about the charge magnitudes or the polarity of net charge in regions without lightning. Furthermore, the distribution of net charge inferred in this way likely underrepresents the complexity of storm electrification, a known bias in all such studies (Brothers et al., 2018; Coleman et al., 2003).
- The heterogeneity of the DLA retrievals are limited by the spatial and temporal resolutions of the radar data set. This might result in the over representation of entrainment at the upstream cloud edge from the underrepresented and relatively discontinuous flow at cloud edge, which in turn would likely reduce the temperature and moisture in the Lagrangian parcels. Dynamical entrainment of dry midtropospheric air is not unphysical, but if it were overrepresented, it would impact the western and southern edges of the storm (i.e., R1) where environmental flow approached the updraft. The spatial averaging on the scale of observed flashes should mitigate lateral differences but could be weighted toward the peripheral environment meaning the cloud water content and temperatures may be larger in R1 (and later R3) than resolved here. If that were so, the isotherms would be at higher altitudes, and both charge layers analyzed in R1 may be more limited to the mixed-phase depths ($\geq 40^{\circ}\text{C}$). This would translate to a deeper column theoretically supportive of NI electrification but would not otherwise affect the resolved charge analysis or associated electrification hypotheses.
- The particle trajectories were mass-weighted trajectories, which does not account for the full spread of trajectories from the whole spectrum of particles that may have ended up at a particular altitude in a given region and contributed to the net charge. The DLA-retrieved fields themselves are based on bulk properties (DiGangi et al., 2016; Ziegler, 2013a, 2013b), similar to the bulk microphysics often used in storm simulation studies including electrification (e.g., Mansell et al., 2013b, 2010), so the associated uncertainties and restrictions of representing all possibilities are similar. This would most likely impact the trajectory analysis in the relatively high reflectivity column of R3, where a large spread in graupel/hail size is possible. This would add large numbers of smaller graupel/hail in the lower charge layers carried around the BWER, relatively more similar to the illustrated snow trajectories (Figure 10), as well as small numbers of larger graupel/hail that would have fallen through larger depths after detraining from the updraft.
- The properties shown at a particular altitude in Figures 7, 9, and 11 were the mean values for all mass-weighted graupel/hail trajectories terminating at that altitude in the region to examine characteristics on the scale of the resulting flashes, so the spectrum of environmental characteristics is also simplified. Variations within these means can be found in the supporting information. The averaging reduces the uncertainty in trajectory path introduced by the resolution of the radar data set but likely oversimplifies the heterogeneity of growth regimes and particle motions in R1 (i.e., Figure S1), where graupel/hail trajectories were more varied along the edge of the strong updraft and charge layers were offset horizontally (as shown in Figures 4c and 4h).

Even with these potential limitations, however, the trajectory analysis was useful in objectively demonstrating the shortcomings of traditional electrification scenarios as particles have a component of their 3-D motion around and through the updraft. In some cases, as we will discuss, the charge found at a particular altitude was consistent with what would have been hypothesized for graupel to gain by NI electrification based on the laboratory experiments by Takahashi (1978), Takahashi and Miyawaki (2002), Saunders et al. (2006), or Emersic and Saunders (2010). In other cases, it simply provided some likely constraints on how the

charge regions could have been produced. The following summarizes our interpretation of the trajectory analyses for each region.

4.1. Region 1

Even with the possibly diluted SLW content from the most significant entrainment and recirculation (e.g., Figure 4), a consistent anomalous charge structure (Figure 7) developed in the updraft core with net positive charge throughout the 6–10 km and 0 to -40°C layer, an inverted dipole. “Diluted” is a relative term as the fast updraft on the western side of the BWER still provided sufficient SLW in nascent graupel/hail containing volumes to be favorable for local positive graupel/hail electrification throughout the midlevels (Bruning et al., 2014; MacGorman et al., 2005; Saunders et al., 2006). What created the upper-negative charge layer is more difficult to ascertain. New positive charge on graupel/hail necessitates negative charge on smaller ice particles. However, the upper-negative charge was present where graupel/hail composed the largest hydrometeor mass near the -40°C layer (Figures 7a and 7c) and sloped over the SLW core (Figure 4h), not constrained to where trajectories of preexisting snow had passed through the net positive charge region minutes earlier on the western side of the BWER (Figure 6). Vertical flux convergence (Figure 7b) would have promoted opportunities for graupel/hail interactions with suddenly increasing concentrations of cloud ice and snow particles (Figure 7d) produced by the rapidly freezing cloud liquid (Figure 7d), while the cold temperatures (Figure 7f) and decreasing SLW content (Figure 7e) could have been favorable for local, recent, negative graupel/hail electrification (e.g., Saunders et al., 2006; Takahashi, 1978). If the upper-negative charge layer was carried on graupel/hail, the production of this anomalous structure would be similar to what was observed over the updraft of the strikingly similar Bruning et al. (2010) storm, but missing the upper layer of positively charged cloud ice, perhaps due to strong downstream advection (Figure 4) of upper-level cloud ice leaving behind too little positive charge to support lightning above the upper-negative charge.

4.2. Region 2

Region R2 contained an inverted tripole structure and particles, which ascended through the primary updraft 10 min prior and were ejected along the northern edge into a persistent, broad midlevel updraft sustaining SLW in the 6- and 10.5-km layer (-7°C to -29°C ; e.g., Figures 5c, 8, and 9) tens of kilometers from the deepest updraft. This environment is expected to be favorable for local NI electrification. The upper levels of the inverted tripole structure (Figures 3 and 9a) throughout this region may reasonably have been generated locally during the descent of existing graupel/hail particles into this layer of mixed-phase precipitation over the previous five minutes (Figures 5c, 5d, 9b, and 9e). Local generation in the previous 5 min for the analyzed R2 column seems especially likely given the history of mixed charge structures along graupel/hail particle trajectories (Figure 9a), the slight downward displacement of the positive charge from the depths containing SLW (Figure 9e), and the expansive area participating in lightning discharges on the northern flank of the storm as discussed by DiGangi et al. (2016).

The lower negative charge layer in R2 contained graupel/hail trajectories tracing both sides of the BWER and interacted with small SLW contents (Figure 8). The trajectories terminating in this layer in R2 at 2348 UTC passed through few grid boxes containing VHF sources (Figure 9a), but those passing cyclonically around the BWER (Figure 8) passed through the same region 10 km to the south, which contains net negative charge in R3 at 2348 UTC (Figure 11) but fewer previous flashes (Figure 3), suggesting the lower charge layer resulted from complex particle advection within the storm, demonstrating a hypothesis presented in the Wiens et al. (2005) case. As with R1, the pattern producing the charge layers in R2 is likely not unique to this storm, as a similar anomalous structure was observed in the forward flank of the Bruning et al. (2010) case, but with a more limited lower charge layer. Small changes in flow may additionally explain how this lower layer was only temporarily present in close proximity to the BWER (Figure 3). These distinct, secondary charge regions may demonstrate that characteristics of the updraft core itself are insufficient to describe the expected charge distribution within a single storm even near the storm core (as hypothesized by Bruning et al., 2014; Wiens et al., 2005). These detailed observations and the DLA capabilities provide updated and detailed observations of such a feature in support of the hypotheses developed from the more limited observations presented in previous cases.

4.3. Region 3

Descending graupel/hail trajectories on the southern periphery of the BWER and contributing to R3 (Figure 10) experienced a different environment than those on the northern side and contributing to R2 (Figures 7, 9, and 11). Reflectivity values and graupel/hail mixing ratios were consistently large at midlevels (Figures 2f–2j and 4), but colocated regions containing updrafts (Figures 2k–2o and 4a–4e) and high flash rates were temporally variable. A deep layer of updraft capable of suspending existing mass-weighted graupel/hail was present on the eastern periphery of the liquid water core at 2348 UTC and coincided with the appearance of a normal tripole charge structure roughly within the 50-dBZ contour and containing a 3-km-deep lower layer of net positive charge (Figures 4c, 4h, and 11). The R3 column was downstream of regions susceptible to cloud-edge entrainment (Figure 10) and consequently colder (Figure 11f) and containing less SLW content (Figure 11e) than R1 or R2 (corresponding panels in Figures 7 and 9), likely favoring negative graupel/hail electrification over the previous 0–2.5 min. Therefore, the midlevel negative charge may have been generated locally by graupel/hail particles contributing to the upper positive layer on snow and ice particles. However, the significant depth of the lower positive layer (Figure 11a) either shows significant transport of charged graupel/hail from the southern periphery of the BWER (Figure 10) or perhaps more extensive SLW than represented by the DLA also enhancing positive graupel/hail electrification locally.

4.4. Concluding Comments

This case first and foremost demonstrates an unusual assortment of charge structures around the core of the storm, showing the sensitivity of storm electrification within small areas. Second, it demonstrates the usefulness of DLA in diagnosing the environment and history along graupel/hail following trajectories, one of the particles expected to carry charge. While charging is not explicitly simulated currently, the native DLA retrievals portray environments favorable for NI electrification. The normal charge structure observed in R3 supports the hypothesis that even within a single storm characterized by an anomalous structure, local pockets of updrafts (e.g., Fuchs et al., 2015; MacGorman et al., 2005) with existing ice particles (MacGorman et al., 2011) can enhance the probability of normal electrification. However, the opposite pattern observed within R2 demonstrates that other factors must still be considered including how SLW content can be sustained at large distances from the primary updraft (e.g., Figure 5c). The uncertainty of how the observed charge structure source over the updraft core in R1 was produced brings into question what should actually be expected in the updraft region of a complex storm, even if the overall structure can be characterized as anomalous.

The similarity of Kingfisher to other storms is an open question. Similar variations in charge regions were observed by Bruning et al. (2010), which suggests that while some of the details of Kingfisher were unexpected, such as the displacement between the BWER and the updraft, it might not be in itself representing any unusual processes or charge redistribution (e.g., Wiens et al., 2005). Since supercells only form in sheared environments, it is possible that entrainment and recirculation of ice and snow upshear of the BWER may commonly provide graupel/hail embryos in strong updrafts supporting SLW at low temperatures and therefore a depth of positive graupel/hail electrification, which might be termed “anomalous.” This electrification structure may or may not be representative of the entire storm given additional zones for particle growth and electrification downshear such as that illustrated by the unusual normal tripole in R3, which might be termed as “anomalous” in this storm. Future studies are needed to determine whether such features are common in storms that meet different overall categorizations to better define what features actually contribute to an overall “anomalous” storm. For example, can a supercell be categorized as “normal” overall but still contain such diversity of vertical charge structures near the BWER? Do they experience similar upshear motions and anomalous charging pockets in conjunction with graupel/hail embryos being (re)introduced to mixed-phase conditions? If so, does the 3-D flow field and hydrometeor habits experienced by particles after exiting the updraft differ? Is there more (or less) diversity in the environments that generate the graupel/hail particles that are advected into the forward flank similar to those in the negative charge layer of R2? Is there simply evidence for less SLW at low temperatures overall? Can observations such as these be used to evaluate the differences of specific NI electrification studies on storm scales (e.g., Glassmeier et al., 2018; Saunders & Peck, 1998; Takahashi, 1978)? Extensions of this methodology to other cases could

begin to answer some of these questions and further inform our theoretical model of storm electrification.

Data Availability Statement

Lightning data are hosted online (at <http://data.eol.ucar.edu/dataset/353.089>). Radar data are hosted at the UCAR website (<https://data.eol.ucar.edu/dataset/353.216>, <http://data.eol.ucar.edu/dataset/353.217>, and <http://data.eol.ucar.edu/dataset/353.215>).

Acknowledgments

This research was performed while the author held an NRC Research Associateship Award at the NOAA National Severe Storms Laboratory. Funding was also provided by NOAA/Office of Oceanic and Atmospheric Research under NOAA-University of Oklahoma Cooperative Agreement NA16OAR4320115, U.S. Department of Commerce. The interpretation of the microphysical growth environments of graupel/hail trajectories via DLA analysis was partially supported by NSF Grant ICER-PREEVENTS-1855100. The radar and lightning data analyzed in this paper were collected by the DC3 field program supported by NSF grant AGS-1063945 and AGS-1063537.

References

- Alford, A. A., Biggerstaff, M. I., Carrie, G. D., Schroeder, J. L., Hirth, B. D., & Waugh, S. M. (2019). Near-surface maximum winds during the landfall of hurricane Harvey. *Geophysical Research Letters*, *46*, 973–982. <https://doi.org/10.1029/2018GL080013>
- Avila, E. E., Saunders, C. P. R., Bax-Norman, H., & Castellano, N. E. (2005). Charge sign reversal in irregular ice particle-graupel collisions. *Geophysical Research Letters*, *32*, L01801. <https://doi.org/10.1029/2004GL020761>
- Baker, B., Baker, M. B., Jayaratne, E. R., Latham, J., & Saunders, C. P. R. (1987). The influence of diffusional growth rates on the charge transfer accompanying rebounding collisions between ice crystals and soft hailstones. *Quarterly Journal of the Royal Meteorological Society*, *113*(478), 1193–1215. <https://doi.org/10.1002/qj.49711347807>
- Barth, M. C., Cantrell, C. A., Brune, W. H., Rutledge, S. A., Crawford, J. H., Huntrieser, H., et al. (2015). The deep convective clouds and chemistry (DC3) field campaign. *Bulletin of the American Meteorological Society*, *96*(8), 1281–1310. <https://doi.org/10.1175/BAMS-D-13-00290.1>
- Biggerstaff, M. I., Wicker, L. J., Guynes, J., Ziegler, C. L., Straka, J. M., Rasmussen, E. N., et al. (2005). The shared mobile atmospheric research and teaching radar. *Bulletin of the American Meteorological Society*, *86*(9), 1263–1274. <https://doi.org/10.1175/BAMS-86-9-1263>
- Brook, M., Nakano, M., Krehbiel, P., & Takeuti, T. (1982). The electrical structure of the Hokuriku winter thunderstorms. *Journal of Geophysical Research*, *87*(C2), 1207–1215. <https://doi.org/10.1016/j.jcosms.2010.07.001>
- Brooks, I. M., Saunders, C. P. R., Mitzeva, R. P., & Peck, S. L. (1997). The effect on thunderstorm charging of the rate of rime accretion by graupel. *Atmospheric Research*, *43*, 277–295.
- Brothers, M. D., Bruning, E. C., & Mansell, E. R. (2018). Investigating the relative contributions of charge deposition and turbulence in organizing charge within a thunderstorm. *Journal of the Atmospheric Sciences*, *75*, 3265–3284. <https://doi.org/10.1175/JAS-D-18-0007.1>
- Bruning, E. C., & MacGorman, D. R. (2013). Theory and observations of controls on lightning flash size spectra. *Journal of the Atmospheric Sciences*, *70*(12), 4012–4029. <https://doi.org/10.1175/JAS-D-12-0289.1>
- Bruning, E. C., Rust, W. D., MacGorman, D. R., Biggerstaff, M. I., & Schuur, T. J. (2010). Formation of charge structures in a supercell. *Monthly Weather Review*, *138*(10), 3740–3761. <https://doi.org/10.1175/2010MWR3160.1>
- Bruning, E. C., Weiss, S. A., & Calhoun, K. M. (2014). Continuous variability in thunderstorm primary electrification and an evaluation of inverted-polarity terminology. *Atmospheric Research*, *135–136*, 274–284. <https://doi.org/10.1016/j.atmosres.2012.10.009>
- Burgess, D. W., Mansell, E. R., Schwarz, C. M., & Allen, B. J. (2010). Tornado and tornadogenesis events seen by the NOXP, X-band, dual-polarization radar during VORTEX2 2010. *Paper presented at 25th AMS Conference on Severe Local Storms*. Paper 5.2. Denver, CO: American Meteorological Society.
- Calhoun, K. M., MacGorman, D. R., Ziegler, C. L., & Biggerstaff, M. I. (2013). Evolution of lightning activity and storm charge relative to dual-Doppler analysis of a high-precipitation supercell storm. *Monthly Weather Review*, *141*(7), 2199–2223. <https://doi.org/10.1175/MWR-D-12-00258.1>
- Calhoun, K. M., Mansell, E. R., Macgorman, D. R., & Dowell, D. C. (2014). Numerical simulations of lightning and storm charge of the 29–30 May 2004 Geary, Oklahoma supercell thunderstorm using EnKF mobile radar data assimilation. *Monthly Weather Review*, *142*, 3977–3997. <https://doi.org/10.1175/MWR-D-13-00403.1>
- Carey, L. D., & Buffalo, K. M. (2007). Environmental control of cloud-to-ground lightning polarity in severe storms. *Monthly Weather Review*, *135*(4), 1327–1353. <https://doi.org/10.1175/MWR3361.1>
- Carey, L. D., & Rutledge, S. A. (1998). Electrical and multiparameter radar observations of a severe hailstorm. *Journal of Geophysical Research*, *103*(D12), 13,979–14,000. <https://doi.org/10.1029/97JD02626>
- Chmielewski, V. C., & Bruning, E. C. (2016). Lightning Mapping Array flash detection performance with variable receiver thresholds. *Journal of Geophysical Research: Atmospheres*, *121*, 8600–8614. <https://doi.org/10.1002/2016JD025159>
- Chmielewski, V. C., Bruning, E. C., & Ancell, B. C. (2018). Variations of thunderstorm charge structures in West Texas on 4 June 2012. *Journal of Geophysical Research: Atmospheres*, *123*, 9502–9523. <https://doi.org/10.1029/2018JD029006>
- Chronis, T., Carey, L. D., Schultz, C. J., Schultz, E. V., Calhoun, K. M., & Goodman, S. J. (2015). Exploring lightning jump characteristics. *Weather and Forecasting*, *30*(1), 23–37. <https://doi.org/10.1175/WAF-D-14-00064.1>
- Coleman, L. M., Marshall, T. C., Stolzenburg, M., Hamlin, T., Krehbiel, P. R., Rison, W., & Thomas, R. J. (2003). Effects of charge and electrostatic potential on lightning propagation. *Journal of Geophysical Research*, *108*(D9), 4298. <https://doi.org/10.1029/2002JD002718>
- DiGangi, E. A. (2019). Observations of evolving lightning, microphysics, and kinematics for a supercell, a multicell, and a mesoscale convective system (Ph.D. Thesis). <https://shareok.org/handle/11244/317788>
- DiGangi, E. A., MacGorman, D. R., Ziegler, C. L., Betten, D., Biggerstaff, M., Bowlan, M., & Potvin, C. K. (2016). An overview of the 29 May 2012 Kingfisher supercell during DC3. *Journal of Geophysical Research: Atmospheres*, *121*, 14,316–14,343. <https://doi.org/10.1002/2016JD025690>
- Dye, J. E., & Bansemmer, A. (2019). Electrification in mesoscale updrafts of deep stratiform and anvil clouds in Florida. *Journal of Geophysical Research: Atmospheres*, *124*, 1021–1049. <https://doi.org/10.1029/2018JD029130>
- Emersic, C., & Saunders, C. P. R. (2010). Further laboratory investigations into the Relative Diffusional Growth Rate theory of thunderstorm electrification. *Atmospheric Research*, *98*, 327–340. <https://doi.org/10.1016/j.atmosres.2010.07.011>
- Fuchs, B. R., Rutledge, S. A., Bruning, E. C., Pierce, J. R., Kodros, J. K., Lang, T. J., et al. (2015). Environmental controls on storm intensity and charge structure in multiple regions of the continental United States. *Journal of Geophysical Research: Atmospheres*, *120*, 6575–6596. <https://doi.org/10.1002/2015JD023271>

- Fuchs, B. R., Rutledge, S. A., Dolan, B., Carey, L. D., & Schultz, C. (2018). Microphysical and kinematic processes associated with anomalous charge structures in isolated convection. *Journal of Geophysical Research: Atmospheres*, *123*, 6505–6528. <https://doi.org/10.1029/2017JD027540>
- Gao, J., Xue, M., Shapiro, A., & Droegemeier, K. K. (1999). A variational method for the analysis of three-dimensional wind fields from two Doppler radars. *Monthly Weather Review*, *127*(9), 2128–2142. [https://doi.org/10.1175/1520-0493\(1999\)127<2128:AVMFTA>2.0.CO;2](https://doi.org/10.1175/1520-0493(1999)127<2128:AVMFTA>2.0.CO;2)
- Glassmeier, F., Arnold, L., Dietlicher, R., Paukert, M., & Lohmann, U. (2018). A modeling study on the sensitivities of atmospheric charge separation according to the relative-diffusional-growth-rate theory to non-spherical hydrometeors and cloud microphysics. *Journal of Geophysical Research: Atmospheres*, *123*, 12,236–12,252. <https://doi.org/10.1029/2018JD028356>
- Helsdon, J. H. Jr., Wu, G., & Farley, R. D. (1992). An intracloud lightning parameterization scheme for a storm electrification model. *Journal of Geophysical Research*, *97*(D5), 5865–5884. <https://doi.org/10.1029/92JD00077>
- Heymsfield, A. J., & Musil, D. J. (1982). Case study of a hailstorm in Colorado. Part II: Particle growth processes at mid-levels deduced from in-situ measurements. *Journal of the Atmospheric Sciences*, *39*(12), 2847–2866. [https://doi.org/10.1175/1520-0469\(1982\)039<2847:CSOAHI>2.0.CO;2](https://doi.org/10.1175/1520-0469(1982)039<2847:CSOAHI>2.0.CO;2)
- Illingworth, A. J., & Latham, J. (1977). Calculations of electric field growth, field structure and charge distributions in thunderstorms. *Quarterly Journal of the Royal Meteorological Society*, *103*, 281–295.
- Kasemir, H. W. (1960). A contribution to the electrostatic theory of a lightning discharge. *Journal of Geophysical Research*, *65*(7), 1873–1878. <https://doi.org/10.1029/JZ065i007p01873>
- Krehbiel, P. R., Rioussel, J. A., Pasko, V. P., Thomas, R. J., Rison, W., Stanley, M. A., & Edens, H. E. (2008). Upward electrical discharges from thunderstorms. *Nature Geoscience*, *1*(4), 233–237. <https://doi.org/10.1038/ngeo162>
- Krehbiel, P. R., Thomas, R. J., Rison, W., Hamlin, T., Harlin, J., & Davis, M. (2000). GPS-based mapping system reveals lightning inside storms. *Eos, Transactions American Geophysical Union*, *81*(3), 21–32. <https://doi.org/10.1029/00EO00014>
- Lang, T. J., Miller, L. J., Weisman, M., Rutledge, S. A., Barker, L. J., Bringi, V. N., et al. (2004). The severe thunderstorm electrification and precipitation study. *Bulletin of the American Meteorological Society*, *85*(8), 1107–1125. <https://doi.org/10.1175/BAMS-85-8-1107>
- Lund, N. R., MacGorman, D. R., Schuur, T. J., Biggerstaff, M. I., & Rust, W. D. (2009). Relationships between lightning location and polarimetric radar signatures in a small mesoscale convective system. *Monthly Weather Review*, *137*(12), 4151–4170. <https://doi.org/10.1175/2009MWR2860.1>
- Luque, M. Y., Bürgesser, R., & Ávila, E. (2016). Thunderstorm graupel charging in the absence of supercooled water droplets. *Quarterly Journal of the Royal Meteorological Society*, *142*(699), 2418–2423. <https://doi.org/10.1002/qj.2834>
- MacGorman, D. R., Apostolopoulos, I. R., Lund, N. R., Demetriades, N. W. S., Murphy, M. J., & Krehbiel, P. R. (2011). The timing of cloud-to-ground lightning relative to total lightning activity. *Monthly Weather Review*, *139*(12), 3871–3886. <https://doi.org/10.1175/MWR-D-11-00047.1>
- MacGorman, D. R., & Burgess, D. W. (1994). Positive cloud-to-ground lightning in tornadic storms and hailstorms. *Monthly Weather Review*, *122*(8), 1671–1697. [https://doi.org/10.1175/1520-0493\(1994\)122<1671:PCTGLI>2.0.CO;2](https://doi.org/10.1175/1520-0493(1994)122<1671:PCTGLI>2.0.CO;2)
- MacGorman, D. R., David Rust, W., Schuur, T. J., Biggerstaff, M. I., Straka, J. M., Ziegler, C. L., et al. (2008). TELEX the thunderstorm electrification and lightning experiment. *Bulletin of the American Meteorological Society*, *89*(7), 997–1013. <https://doi.org/10.1175/2007BAMS2352.1>
- MacGorman, D. R., Elliott, M. S., & DiGangi, E. (2017). Electrical discharges in the overshooting tops of thunderstorms. *Journal of Geophysical Research: Atmospheres*, *122*, 2929–2957. <https://doi.org/10.1002/2016JD025933>
- MacGorman, D. R., Few, A. A., & Teer, T. L. (1981). Layered lightning activity. *Journal of Geophysical Research*, *86*(C10), 9900–9910.
- MacGorman, D. R., Rust, W. D., Krehbiel, P., Rison, W., Bruning, E., & Wiens, K. (2005). The electrical structure of two supercell storms during STEPS. *Monthly Weather Review*, *133*(9), 2583–2607. <https://doi.org/10.1175/MWR2994.1>
- MacGorman, D. R., Straka, J. M., & Ziegler, C. L. (2001). A lightning parameterization for numerical cloud models. *Journal of Applied Meteorology*, *40*(3), 459–478. [https://doi.org/10.1175/1520-0450\(2001\)040<0459:ALPFNC>2.0.CO;2](https://doi.org/10.1175/1520-0450(2001)040<0459:ALPFNC>2.0.CO;2)
- Maggio, C., Coleman, L., Marshall, T., Stolzenburg, M., Stanley, M., Hamlin, T., et al. (2005). Lightning-initiation locations as a remote sensing tool of large thunderstorm electric field vectors. *Journal of Atmospheric and Oceanic Technology*, *22*(7), 1059–1068. <https://doi.org/10.1175/JTECH1750.1>
- Mansell, E. R., MacGorman, D. R., Ziegler, C. L., & Straka, J. M. (2005). Charge structure and lightning sensitivity in a simulated multicell thunderstorm. *Journal of Geophysical Research*, *110*, D12101. <https://doi.org/10.1029/2004JD005287>
- Mansell, E. R., Ziegler, C. L., & Bruning, E. C. (2010). Simulated electrification of a small thunderstorm with two-moment bulk microphysics. *Journal of the Atmospheric Sciences*, *67*(1), 171–194. <https://doi.org/10.1175/2009JAS2965.1>
- Marshall, T. C., & Stolzenburg, M. (2002). Electrical energy constraints on lightning. *Journal of Geophysical Research*, *107*(D7), 4052. <https://doi.org/10.1029/2000JD000024>
- Mazur, V., & Ruhnke, L. H. (1993). Common physical processes in natural and artificially triggered lightning. *Journal of Geophysical Research*, *98*(D7), 12,913–12,930. <https://doi.org/10.1029/93JD00626>
- Miller, L. J., Tuttle, J. D., & Knight, C. A. (1988). Airflow and hail growth in a severe Northern High Plains supercell. *Journal of the Atmospheric Sciences*, *45*(4), 736–762.
- Musil, D. J., Heymsfield, A. J., & Smith, P. L. (1986). Microphysical characteristics of a well-developed weak echo region in a High Plains supercell thunderstorm. *Journal of Climate and Applied Meteorology*, *25*, 1037–1051. [https://doi.org/10.1175/1520-0450\(1986\)025<1037:MCOAWD>2.0.CO;2](https://doi.org/10.1175/1520-0450(1986)025<1037:MCOAWD>2.0.CO;2)
- Oye, R. A., Mueller, C., & Smit, S. (1995). Software for the radar translation, visualization, editing, and interpolation. *Paper presented at 27th Conference on Radar Meteorology* (pp. 359–361). Vail, CO: American Meteorological Society.
- Payne, C. D., Schuur, T. J., MacGorman, D. R., Biggerstaff, M. I., Kuhlman, K. M., & Rust, W. D. (2010). Polarimetric and electrical characteristics of a lightning ring in a supercell storm. *Monthly Weather Review*, *138*(6), 2405–2425. <https://doi.org/10.1175/2009MWR3210.1>
- Potvin, C. K., Wicker, L. J., & Shapiro, A. (2012). Assessing errors in variational dual-Doppler wind syntheses of supercell thunderstorms observed by storm-scale mobile radars. *Journal of Atmospheric and Oceanic Technology*, *29*(8), 1009–1025. <https://doi.org/10.1175/JTECH-D-11-00177.1>
- Rison, W., Krehbiel, P. R., Stock, M. G., Edens, H. E., Shao, X.-M., Thomas, R. J., et al. (2016). Observations of narrow bipolar events reveal how lightning is initiated in thunderstorms. *Nature Communications*, *7*, 10,721. <https://doi.org/10.1038/ncomms10721>
- Rust, W. D., & MacGorman, D. R. (2002). Possibly inverted-polarity electrical structures in thunderstorms during STEPS. *Geophysical Research Letters*, *29*(12), 1571. <https://doi.org/10.1029/2001GL014303>

- Rust, W. D., MacGorman, D. R., Bruning, E. C., Weiss, S. A., Krehbiel, P. R., Thomas, R. J., et al. (2005). Inverted-polarity electrical structures in thunderstorms in the Severe Thunderstorm Electrification and Precipitation Study (STEPS). *Atmospheric Research*, *76*(1-4), 247–271. <https://doi.org/10.1016/j.atmosres.2004.11.029>
- Saunders, C. P. R., Bax-norman, H., Emersic, C., Avila, E. E., & Castellano, N. E. (2006). Laboratory studies of the effect of cloud conditions on graupel/crystal charge transfer in thunderstorm electrification. *Quarterly Journal of the Royal Meteorological Society*, *132*, 2653–2673. <https://doi.org/10.1256/qj.05.218>
- Saunders, C. P. R., & Peck, S. L. (1998). Laboratory studies of the influence of the rime accretion rate on charge transfer during crystal/graupel collisions. *Journal of Geophysical Research*, *103*(D12), 13,949–13,956. <https://doi.org/10.1029/97JD02644>
- Schultz, C. J., Carey, L. D., Schultz, E. V., & Blakeslee, R. J. (2015). Insight into the kinematic and microphysical processes that control lightning jumps. *Weather and Forecasting*, *30*, 1591–1621. <https://doi.org/10.1175/WAF-D-14-00147.1>
- Shao, X. M., & Krehbiel, P. R. (1996). The spatial and temporal development of intracloud lightning. *Journal of Geophysical Research*, *101*(D21), 26,641–26,668. <https://doi.org/10.1029/96JD01803>
- Shapiro, A., Potvin, C. K., & Gao, J. (2009). Use of a vertical vorticity equation in variational dual-doppler wind analysis. *Journal of Atmospheric and Oceanic Technology*, *26*(10), 2089–2106. <https://doi.org/10.1175/2009JTECHA1256.1>
- Sibson, R. (1981). A brief description of natural neighbor interpolation, *Interpreting multivariate data* (pp. 21–36). New York: John Wiley.
- Simpson, G., & Robinson, G. D. (1941). The distribution of electricity in thunderclouds, II. *Proceedings of the Royal Society of London. Series A, Mathematical and Physical Sciences*, *177*, 281–329. <https://doi.org/10.1098/rspa.1974.0120>
- Stolzenburg, M., Rust, W. D., & Marshall, T. C. (1998). Electrical structure in thunderstorm convective regions: 2. Isolated storms. *Journal of Geophysical Research*, *103*(D12), 14,079–14,096.
- Straka, J. M., & Mansell, E. R. (2005). A bulk microphysics parameterization with multiple ice precipitation categories. *Journal of Applied Meteorology*, *44*, 445–466. <https://doi.org/10.1175/JAM2211.1>
- Takahashi, T. (1978). Riming electrification as a charge generation mechanism in thunderstorms. *Journal of the Atmospheric Sciences*, *35*, 1536–1548. [https://doi.org/10.1175/1520-0469\(1978\)035<1536:REAACG>2.0.CO;2](https://doi.org/10.1175/1520-0469(1978)035<1536:REAACG>2.0.CO;2)
- Takahashi, T., & Miyawaki, K. (2002). Reexamination of riming electrification in a wind tunnel. *Journal of the Atmospheric Sciences*, *59*, 1018–1025. [https://doi.org/10.1175/1520-0469\(2002\)059<1018:ROREIA>2.0.CO;2](https://doi.org/10.1175/1520-0469(2002)059<1018:ROREIA>2.0.CO;2)
- Tessendorf, S. A., Rutledge, S. A., & Wiens, K. C. (2007). Radar and lightning observations of normal and inverted polarity multicellular storms from STEPS. *Monthly Weather Review*, *135*(11), 3682–3706. <https://doi.org/10.1175/2007MWR1954.1>
- Thomas, R. J., Krehbiel, P. R., Rison, W., Hamlin, T., Harlin, J., & Shown, D. (2001). Observations of VHF source powers radiated by lightning. *Geophysical Research Letters*, *28*(1), 143–146. <https://doi.org/10.1029/2000GL01464>
- Thomas, R. J., Krehbiel, P. R., Rison, W., Hunyady, S. J., Winn, W. P., Hamlin, T., & Harlin, J. (2004). Accuracy of the lightning mapping array. *Journal of Geophysical Research*, *109*, D14207. <https://doi.org/10.1029/2004JD004549>
- Tsenova, B. D., & Mitzeva, R. P. (2009). New parameterization of non-inductive charge transfer based on previous laboratory experiments. *Atmospheric Research*, *91*, 79–86. <https://doi.org/10.1016/j.atmosres.2008.07.001>
- van der Velde, O. A., & Montanyà, J. (2013). Asymmetries in bidirectional leader development of lightning flashes. *Journal of Geophysical Research: Atmospheres*, *118*, 13,504–13,519. <https://doi.org/10.1002/2013JD020257>
- Waugh, S. M. (2016). A balloon-borne particle size, imaging, and velocity probe for in situ microphysical measurements (Ph.D. Thesis). <https://hdl.handle.net/11244/45407>
- Waugh, S. M., Ziegler, C. L., & MacGorman, D. R. (2018). In situ microphysical observations of the 29-30 May 2012 Kingfisher, OK, supercell with a balloon-borne video disdrometer. *Journal of Geophysical Research: Atmospheres*, *123*, 1–23. <https://doi.org/10.1029/2017JD027623>
- Wiens, K. C., Rutledge, S. A., & Tessendorf, S. A. (2005). The 29 June 2000 supercell observed during STEPS. Part II: Lightning and charge structure. *Journal of the Atmospheric Sciences*, *62*(12), 4151–4177. <https://doi.org/10.1175/JAS3615.1>
- Williams, E. R., Cooke, C. M., & Wright, K. A. (1985). Electrical discharge propagation in and around space charge clouds. *Journal of Geophysical Research*, *90*(D4), 6059–6070. <https://doi.org/10.1029/JD090iD04p06059>
- Williams, E., Mushtak, V., Rosenfeld, D., Goodman, S., & Boccippio, D. (2005). Thermodynamic conditions favorable to superlative thunderstorm updraft, mixed phase microphysics and lightning flash rate. *Atmospheric Research*, *76*(1-4), 288–306. <https://doi.org/10.1016/j.atmosres.2004.11.009>
- Ziegler, C. L. (2013a). A diabatic Lagrangian technique for the analysis of convective storms. Part I: Description and validation via an observing system simulation experiment. *Journal of Atmospheric and Oceanic Technology*, *30*(10), 2248–2265. <https://doi.org/10.1175/JTECH-D-12-00194.1>
- Ziegler, C. L. (2013b). A diabatic Lagrangian technique for the analysis of convective storms. Part II: Application to a radar-observed storm. *Journal of Atmospheric and Oceanic Technology*, *30*(10), 2266–2280. <https://doi.org/10.1175/JTECH-D-13-00036.1>
- Ziegler, C. L., MacGorman, D. R., Dye, J. E., & Ray, P. S. (1991). A model evaluation of noninductive graupel-ice charging in the early electrification of a mountain thunderstorm. *Journal of Geophysical Research*, *96*(D7), 12,833–12,855. <https://doi.org/10.1029/91JD01246>
- Ziegler, C. L., Mansell, E. R., Calhoun, K. M., & MacGorman, D. R. (2014). Impact of kinematics, microphysics, and electrification on the formation of lightning-weak holes in a simulated supercell storm. *Paper presented at 15th International Conference on Atmospheric Electricity* (pp. 0–16). Norman, OK: International Commission on Atmospheric Electricity.
- Ziegler, C. L., Ray, P. S., & Knight, N. C. (1983). Hail growth in an Oklahoma multicell storm. *Journal of the Atmospheric Sciences*, *40*(7), 1768–1791. [https://doi.org/10.1175/1520-0469\(1983\)040<1768:HGAOM>2.0.CO;2](https://doi.org/10.1175/1520-0469(1983)040<1768:HGAOM>2.0.CO;2)
- Ziegler, C. L., Ray, P. S., & MacGorman, D. R. (1986). Relations of kinematics, microphysics and electrification in an isolated mountain thunderstorm. *Journal of the Atmospheric Sciences*, *43*(19), 2098–2114. [https://doi.org/10.1175/1520-0469\(1986\)043<2098:rokmae>2.0.co;2](https://doi.org/10.1175/1520-0469(1986)043<2098:rokmae>2.0.co;2)